ROYAL SOCIETY OF CHEMISTRY

CRITICAL REVIEW

Check for updates

Low-temperature plasma-enabled CO_2 dissociation: a critical analysis of plasma setups and conversion mechanisms toward scale-up valorization

Yuxuan Xu, [ID] [a,b] Yuan Gao, [ID] [a] Liguang Dou, [ID] [a] Dengke Xi, [ID] [a] Chong Qi, [ID] [a,b] Baowang Lu [ID] [c] and Tao Shao [ID] *[a,b]

CO_2 dissociation, as one of the key pathways for carbon utilization, plays a critical role in sustainable carbon emission reduction. Low-temperature plasma (LTP) technology, with its highly reactive characteristics, can effectively lower the energy barrier for CO_2 activation, thus facilitating efficient CO_2 dissociation with reduced energy requirement. LTP-enabled CO_2 dissociation has attracted widespread research interests aiming to enhance conversion performance and advance scale-up applications in recent years. Achieving such an objective necessitates dual-level considerations from both the plasma setups, such as power supplies, *in situ* and post-treatment control strategies, and the conversion mechanisms which encompass insights from diagnostic techniques, reaction kinetics simulations, and multi-physics modeling. Following an overview of the basic characteristics of different plasma systems and the distinctions between the CO_2 dissociation processes driven by thermal catalysis and plasma catalysis, this review examines the current developments and existing limitations in LTP setups and conversion mechanisms through comprehensive analyses of experimental achievements and mechanistic investigations in LTP-enabled CO_2 dissociation. Based on these findings, we propose a strategic outlook for the progression of LTP-enabled CO_2 valorization from laboratory research toward scale-up implementations.

Green foundation

1. This review explores recent developments in low-temperature plasma technology as an innovative green energy conversion method for CO_2 dissociation, focusing on the status and limitations of plasma setups and conversion mechanisms.

2. Low-temperature plasma-enabled CO_2 dissociation represents a crucial sustainable carbon emission reduction strategy. Leveraging the capability of efficient CO_2 valorization, it holds promising potential for broader applications across various carbon emission scenarios.

3. Future advancements require synergistic optimization of CO_2 conversion performance and techno-economic feasibility for scale-up implementations. Through comparative analysis of various plasma technologies, this review provides critical guidance for facilitating holistic process optimization and maturation of plasma-enabled CO_2 dissociation systems, ultimately contributing to the establishment of sustainable carbon cycling infrastructures aligned with green chemistry principles.

Introduction

Efficient utilization of greenhouse gases, especially CO_2, is one of the most powerful strategies to address the global warming challenge before realizing the strategic goals of "carbon peaking" and "carbon neutrality".[1–5] Although the physical methods of CO_2 utilization, such as in the enhanced oil recovery industry, have advanced to a mature stage, they lack the

[a]Beijing International S&T Cooperation Base for Plasma Science and Energy Conversion, Institute of Electrical Engineering, Chinese Academy of Sciences, Beijing 100190, China. E-mail: st@mail.iee.ac.cn
[b]University of Chinese Academy of Sciences, Beijing 100049, China
[c]National Institute of Clean-and-Low-Carbon Energy, Beijing 102211, China

sustainable development momentum to leverage economic benefits.[6–9] On the other hand, chemical utilization of CO_2 targeting value-added chemicals has emerged as a promising alternative in recent years.[10,11] Aligned with the trend of transitioning to green and renewable energy,[12–14] the chemical approach not only holds the potential for achieving "net-zero" emissions[15–17] through "artificial carbon cycling",[18,19] but also paves the way for vast application possibilities for the valorization of CO_2 (Power-to-X, P2X).[20–24] Among all the CO_2-related P2X technologies, direct CO_2 dissociation (R1) is the simplest route for value-added utilization, as it allows one-step conversion of chemically inert CO_2 molecules (with a C=O bond energy of 783 kJ·mol^{-1}) into CO. The CO product, in turn, can serve as a precursor for various important platform chemicals

such as formaldehyde and methanol,[25–27] making this reaction the subject of extensive research. However, due to the inherent stability of the CO_2 molecule, this reaction generally requires a high energy input along with the use of catalysts and specific environmental conditions.[28–30] Throughout extensive exploration, the well-established conversion techniques commonly employed for CO_2 dissociation are thermal catalysis and electrocatalysis. While both methods have made certain breakthroughs in terms of conversion rate and energy efficiency, the reliance on expensive metal catalysts and the need for stable CO_2 sources and energy supplies have limited their adaptability in many CO_2 emission reduction scenarios.[31–40]

$$CO_2(g) \rightarrow CO(g) + \frac{1}{2}O_2(g), \quad \Delta H = 283 \text{ kJ mol}^{-1} \quad (1)$$
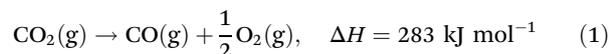
Low-temperature plasma (LTP) technology, as a novel energy conversion pathway, represents an important alternative for CO_2 conversion.[41,42] The LTP is a multi-component system, with numerous charged and neutral species co-existing at different temperatures. The thermal equilibrium state of LTP can be assessed by examining the electron temperature (T_e) and the gas temperature (T_g).[43,44] Typically, LTP is in a non-thermal equilibrium state, where $T_e \gg T_g$. In terms of CO_2 activation mechanisms, LTP can generate high-energy electrons (1–10 eV) and reactive species under limited energy input, thereby reducing the activation energy for CO_2 dissociation without the need for catalysts.[45,46] Regarding its application prospects, LTP-based CO_2 dissociation, as an electric-driven reaction process with "instant-on/off" characteristics, is well suited for coupling with intermittent renewable energy sources, contributing to distributed and flexible CO_2 utilization.[47–51] Furthermore, considering that CO_2 dissociation does not involve intricate reaction pathways in multi-reactant systems,[52–54] the issue of product selectivity in plasma discharge processes is often minimal, making it highly valu-able for both research and practical deployment in CO_2 dissociation approaches.

Nevertheless, after examining a substantial amount of research on LTP-enabled CO_2 dissociation, it has been observed that while many experimental results demonstrate high CO_2 dissociation conversion rates, the corresponding energy efficiency still lacks sufficient competitiveness.[55–57] Hence, balancing conversion with energy consumption is one of the key challenges in advancing LTP technology from the laboratory level to scale-up applications.[58–60] Existing improvement strategies typically focus on reactor modifications,[61,62] optimization of reaction parameters,[63,64] and the design of plasma-specific catalysts,[65,66] all of which are out of iterations within a specific plasma form. Yet, the absence of comparisons of different LTP-enabled CO_2 dissociation pathways should provide new insights into addressing the aforementioned challenges from a holistic perspective.

Based on a comprehensive investigation of the current status, advantages, and drawbacks of various LTP-enabled CO_2 dissociation approaches, this work provides a detailed analysis of the macroscopic plasma setups and the microscopic CO_2 dissociation mechanisms. The former directly impacts CO_2 conversion performance but is constrained by the core reaction steps within the latter, which suggests an interacting relationship. On top of that, we further discuss the technological bottlenecks that need to be overcome for the outlook toward industrial-scale applications of LTP-enabled CO_2 dissociation.

LTP systems for CO_2 dissociation

Due to variations in the types of power supplies and reactors, several forms of LTP can be produced. The LTP types commonly employed in the field of CO_2 dissociation include dielectric barrier discharge (DBD) plasma, gliding arc dis-

Yuxuan Xu obtained a B.E. degree in Electrical Engineering and Automation from the Department of Electrical Engineering, Tsinghua University in 2021. He is currently pursuing his Ph.D. degree at the Institute of Electrical Engineering, Chinese Academy of Sciences. His research mainly focuses on low-temperature plasma-enabled CO_2 conversion into value-added chemicals.

Yuxuan Xu

Tao Shao received an M.Sc. degree in Electrical Engineering from Wuhan University in 2003, and a Ph.D. degree in Electrical Engineering from the University of the Chinese Academy of Sciences (CAS) in 2006. He then joined the Institute of Electrical Engineering, CAS, and was promoted to Professor of the Institute in 2013. His current research interests include high-voltage breakdown and insulation, gas discharge physics, and plasma applications. Dr Shao was awarded the Royal Society-Newton Advanced Fellowship (NA140303) in 2015 and received the 2025 IEEE Magne "Kris" Kristiansen award. He also chaired the 2024 IEEE International Conference on Plasma Science.

Tao Shao

charge (GAD) plasma, microwave discharge (MWD) plasma, and spark discharge plasma. Additionally, some studies have also explored the use of corona discharge plasma, glow discharge plasma, and radio frequency (RF) discharge plasma to effectively dissociate CO_2. Given the distinct CO_2 activation characteristics of these plasma systems, it is essential to understand the features of each type of plasma configuration, which will be introduced below.

DBD plasma

DBD plasma is typically initiated between electrodes filled with dielectric materials, and its typical reactor structure is shown in Fig. 1(a). The cylindrical high-voltage (HV) electrode at the center of this coaxial reactor and the surrounding ground electrode generate a high electric field within the discharge gap. The external dielectric (usually quartz), the gas (CO_2 and/or carrier gases) introduced into the discharge gap, the packing materials, and the internal dielectric material attached to the surface of the HV electrode collectively affect the discharge characteristics with their different dielectric properties. When the applied electric field reaches the breakdown threshold, the discharge is generated in the gap region,

thereby leading to the formation of DBD plasma. Due to the current-limiting effect of the dielectric barrier, the discharge channel is prevented from transitioning into a spark mode. As a result of varying electron mean free paths and space charge effects, DBD plasma discharge can achieve uniform diffuse discharge at low pressures, whilst at atmospheric pressure, it manifests as filamentary discharge. If the external dielectric in Fig. 1(a) is replaced by parallel plate-shaped HV and ground electrodes, and the central HV electrode is replaced by a dielectric material, another commonly used parallel plate-electrode DBD reactor structure is formed. Since the heating effect of DBD plasma is insignificant, the wall temperature of the reactor during operation typically remains below 500 K. In the above structures, the packing materials can be added into the gas gap to achieve a synergistic effect with LTP. Upon integration with catalysts as packing materials, it not only lowers the activation energy for CO_2 dissociation but also modulates the dielectric properties, thereby enhancing plasma discharge and increasing the CO_2 conversion rate. This is also one of the unique advantages of DBD plasma.

From the perspective of discharge characteristics, DBD plasma exhibits non-equilibrium properties with significantly
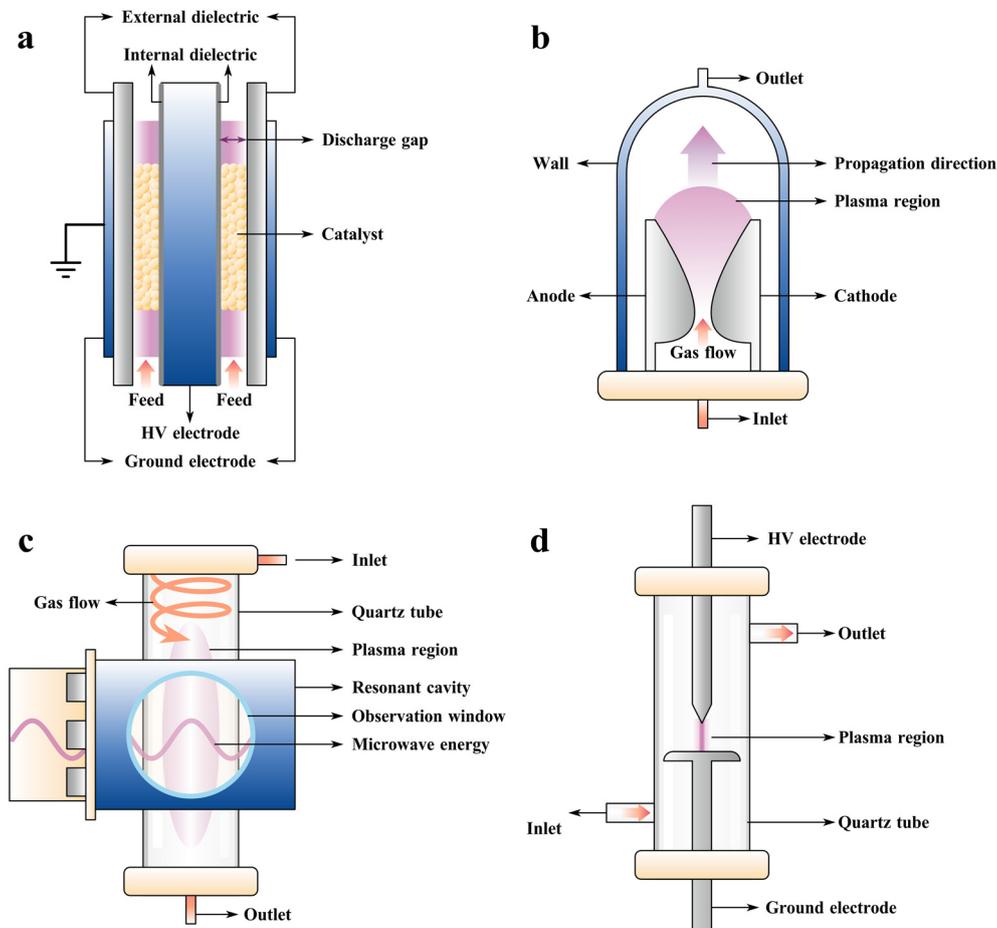

Fig. 1 Typical schematic view of different plasma reactors applied in CO_2 dissociation. (a) A DBD plasma reactor. (b) A GAD plasma reactor. (c) An MWD plasma reactor. (d) A spark discharge plasma reactor.

different vibrational temperature (T_v) and rotational temperature (T_r). Under the high reduced electric field (E/n) of several hundred Townsends (T_d), a large amount of power is used to generate high-energy electrons, which trigger the electronic excitation and dissociative ionization of ground-state CO_2 molecules. Such reaction pathways limit the energy efficiency of CO_2 dissociation in DBD plasma. Moreover, in order to maintain stable and uniform discharge while ensuring sufficient interaction between CO_2 molecules and the catalysts for high conversion rates, the throughput of the DBD plasma process is often limited.

GAD plasma

GAD plasma is also commonly used in CO_2 dissociation studies. GAD can be initiated through a blade-electrode structure, as shown in Fig. 1(b). The high electric field between the two electrodes generates an arc channel, which then evolves into GAD under its gas-heating effect and the high-speed gas flow. Compared to DBD, GAD is more intense, and the plasma region reaches a higher thermal equilibrium state. The high T_g (>1000 K) in the discharge channel makes the *in situ* coupling with catalysts quite challenging. Notably, the CO_2 dissociation pathway shifts from electron-induced excitation and dissociation in DBD plasma to the vibrational excitation process in GAD. It subsequently forms vibrationally excited CO_2 molecules with higher energy states through vibrational–vibrational (V–V) collisions which further participate in the dissociation process. This reaction pathway utilizes lower electron energies (<5.5 eV) to excite CO_2 dissociation, effectively reducing the energy consumption of CO_2 dissociation in GAD plasma.[67] However, in typical situations of large gas flow rates in GAD plasma systems, the insufficient contact time between CO_2 and the plasma channel limits its conversion level.

In addition to the GAD reactor structure with quasi-two-dimensional blade electrodes, some studies have designed three-dimensional multi-blade electrodes[68] and rotating GAD (RGAD) plasma reactors.[69] Expanding the plasma region is considered beneficial for increasing the residence time of reactant gases, which can enhance the CO_2 dissociation conversion in GAD plasma to some extent. Another approach to improve CO_2 conversion is catalyst integration in the post-plasma region of the reactor, where the residual heat downstream of the discharge channel further ignites the catalysts to facilitate the conversion of unreacted CO_2 molecules.

MWD plasma

MWD plasma is generated by electromagnetic waves of specific frequencies (such as 915 MHz or 2.45 GHz) that create a high electric field in a resonant cavity, with no typical requirement for electrodes. As shown in Fig. 1(c), MWD plasma reactors typically feature a passive discharge structure, where the microwave energy directly induces discharge in the quartz tube by reflection and resonance within the resonant cavity. When operated under low pressure, MWD plasma exhibits a uniform diffuse discharge mode. As the pressure increases, the discharge region gradually contracts, evolving into the form of a plasma torch. Compared to the previous two plasma types, MWD plasma produces electrons with lower energy levels (<1 eV), accompanied by further improvement in thermal equilibrium. For CO_2 dissociation reactions, under certain low-pressure operating conditions, the dissociation pathway primarily follows CO_2 vibrational excitation. However, the pathways dominated by thermal effects, such as heavy particles or high-energy electrons collision, become more prominent in many circumstances of MWD plasma studies. Meanwhile, the reverse reaction issue emerges as one of the bottlenecks limiting the enhancement of CO_2 conversion performance.

To suppress the post-plasma temperature of MWD systems, the addition of a downstream quenching structure (such as a converging-diverging nozzle, CDN) can improve heat distribution through altering the flow velocity, ensuring that the temperature downstream the core discharge region remains outside the temperature range of thermal equilibrium, thereby reducing the extent of reverse reactions. Additionally, besides coupling catalysts in the post-plasma region, similar to the approach used in GAD plasma, some studies have also explored the coupling of MWD plasma with electrocatalysis to enhance the overall conversion of CO_2 dissociation.[70]

Spark discharge plasma

Spark discharge plasma is typically initiated and sustained by a high electric field between appropriately spaced electrodes, with its typical reactor structure shown in Fig. 1(d). From the perspective of discharge voltage-current characteristics, during a spark discharge cycle, the voltage amplitude decreases and then slowly recovers, while the channel current rapidly rises to the ampere-level and reverses, followed by oscillatory decay near the zero-crossing point. This electrical behavior results in a relatively insignificant accumulation of thermal effects in the spark discharge channel.

With regard to the CO_2 dissociation reaction pathway, the vibrational excitation process remains dominant in spark discharge plasma, offering advantages in balancing the conversion rate and energy efficiency. However, due to the relatively small volume of the spark discharge channel within the reactor, enhancing the contact between CO_2 reactants and the discharge region, as well as improving the conversion level within the discharge channel, represents an important research breakthrough. Some studies have pointed out that, compared to the quasi-uniform electric fields generated by plate and arc-shaped electrode structures, utilizing the highly non-uniform electric field created by the needle-plate electrode configuration, as shown in Fig. 1(d), can yield better CO_2 dissociation conversion results.[71]

Other plasma types

In addition to the plasma forms mentioned above, there are also studies utilizing corona discharge, glow discharge, non-self-sustained discharge, RF discharge, and other types of plasma for CO_2 dissociation. Among the first three plasma forms, several experiments report relatively high conversion rates (up to 30%),[72] but they often require the addition of

carrier gases such as He for elevated electron density or operation under low-pressure conditions to maintain stable discharge. On the other hand, RF discharge plasma, like MWD plasma in terms of electromagnetic excitation principles, can achieve high CO_2 conversion rates (up to 80%),[73] but the energy efficiency remains insufficient to meet the requirements for further scaling up and widespread applications.

Fundamentals of CO_2 dissociation

Thermal catalysis

Understanding the thermal catalytic dissociation mechanisms of CO_2 is crucial for clarifying the key intermediate steps in the CO_2 dissociation process and identifying the limiting factors affecting conversion performance. As an endothermic elementary reaction, CO_2 dissociation requires extremely high temperatures when only the thermal effects are taken into account. The theoretical calculations shown in Fig. 2(a) indicate that, in a closed adiabatic system at atmospheric pressure, under initial conditions at 298.15 K, CO_2 molecules do not undergo significant dissociation when the temperature is below 2000 K. As the temperature gradually increases from 2000 K to 4000 K, CO_2 begins to dissociate, generating gaseous CO and O_2 molecules, with the ratio of their production always being maintained at 2 : 1. When the temperature reaches around 5000 K, CO_2 completely dissociates, leaving only two gaseous products (CO and O_2). However, when the temperature further increased to above 7000 K, CO molecules begin to decompose (R2), generating gaseous carbon (C) and O_2. In practice, due to kinetic limitations, it is not possible to achieve further dissociation of CO in the CO_2 dissociation system by simply raising the temperature. Typically, CO must first adsorb onto the surfaces of metal crystals such as Fe[74] and Co[75] to be activated before dissociation can occur.

$$CO(g) \rightarrow C(g) + \frac{1}{2}O_2(g), \quad \Delta H = 824 \text{ kJ mol}^{-1} \quad (2)$$
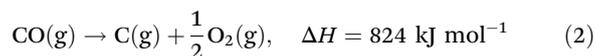
The addition of catalysts can significantly lower the operating temperature required for the thermal dissociation of CO_2. Through the specific structural design of catalysts and the Langmuir–Hinshelwood (L–H) mechanism of reactant molecules on the catalyst surface, the activation energy for CO_2 dissociation is substantially reduced, allowing the dissociation reaction to occur at temperatures well below those predicted by theoretical calculations. Liu et al.[76] prepared a Cu(I)/TiO$_{2-x}$ catalyst with oxygen vacancies by pretreating it under a He atmosphere. At room temperature, CO_2 molecules undergo a series of processes: surface adsorption, electron transfer, capture of oxygen atoms from CO_2 by oxygen vacancies, formation and breaking of Cu$^+$–CO bonds, and finally, the desorption of CO from the surface, completing the dissociation process. Fig. 2(b) illustrates a schematic of these key steps.
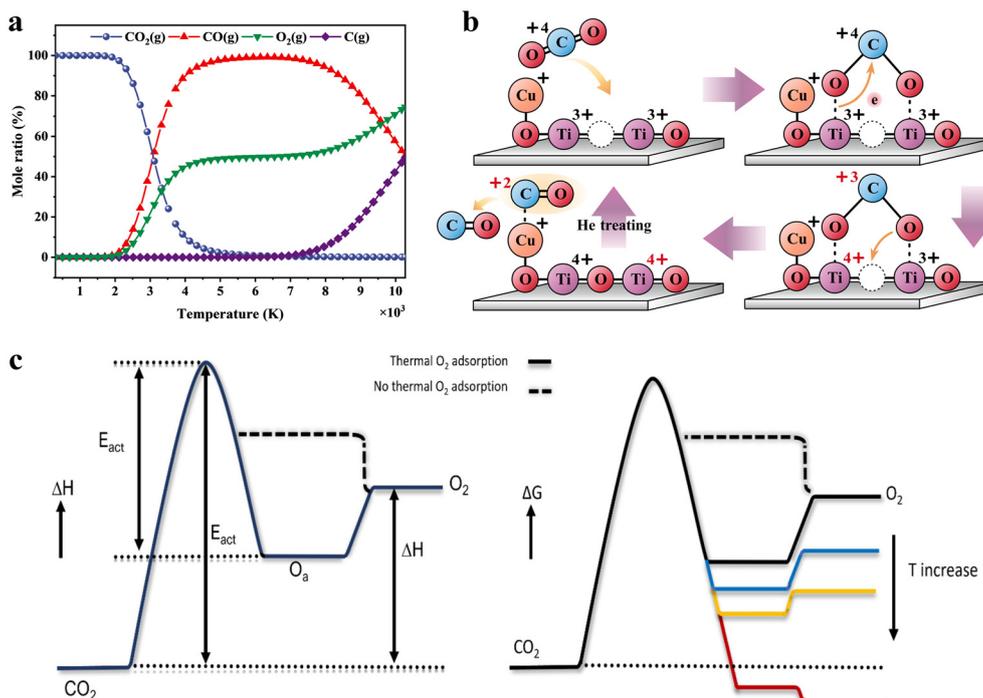

Fig. 2 Thermal catalysis of CO_2 dissociation. (a) Calculated mole fraction of the main molecules in CO_2 dissociation with increase in temperature. (b) A typical thermal catalysis process of CO_2 dissociation on the Cu(I)/TiO$_{2-x}$ surface. Reproduced from ref. 76 with permission from the American Chemical Society, copyright 2012. (c) Qualitative enthalpy and Gibbs energy plots presenting a basic two step mechanism of thermal-catalytic CO_2 dissociation. Reproduced from ref. 77 with permission from John Wiley and Sons, copyright 2024.

To better understand the CO_2 thermal catalytic reaction process, Lefferts[77] explored two key reaction steps after the introduction of catalysts:

$$CO_2 + es \rightarrow CO + O_{ads} \qquad (3)$$

$$2O_{ads} \leftrightarrow O_2 + 2es \qquad (4)$$

In the above equation, "es" represents the vacancy, and "O_{ads}" represents the adsorbed oxygen atom. Since the adsorption of CO on the metal surface is generally weaker than the dissociative adsorption of O_2 molecules,[78,79] the adsorption state of CO is typically not considered. The dissociative adsorption of CO_2 on the catalyst surface in reaction R3 is the rate-limiting step. If this process is reversible, the composite reaction (R5) must be considered to obtain the actual reaction rate of R3. The desorption of dissociatively adsorbed oxygen atoms (R4) is always at dynamic equilibrium, with its reaction rate constant equal to the inverse of the dissociative adsorption rate constant of O_2 on the catalyst surface.

$$CO + O_{ads} \rightarrow CO_2 + es \qquad (5)$$
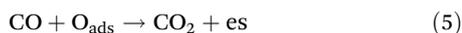
If the catalyst has a strong dissociative adsorption effect on O_2, the reaction rate constant for R4 is much smaller than 1, meaning that the active sites of the catalyst surface are largely occupied, which suppresses the rate of R3. On the other hand, when the catalyst has a weak dissociative adsorption effect on O_2, the reaction rate constant for R4 is much greater than 1, and the rate of R3 primarily depends on the concentration of CO_2 molecules in the gas phase.

In terms of qualitative changes in reaction enthalpy and Gibbs free energy depicted in Fig. 2(c), the solid black line represents the CO_2 dissociation process on the catalyst surface that has a dissociative adsorption effect on O_2. After overcoming the activation energy barrier for CO_2, it enters the O_{ads} state, which requires further overcoming of the energy barrier from O_{ads} to O_2. The dashed black line, on the other hand, represents the reaction process on the catalyst surface with a weak dissociative adsorption effect on O_2. After the CO_2 dissociative adsorption, it directly transitions to O_2 without going through the O_{ads} state. The corresponding change in Gibbs free energy reveals that the transition from the dashed black line to O_2 is spontaneous ($\Delta G < 0$), while the transition from O_{ads} to O_2 on the solid black line has a positive Gibbs free energy change ($\Delta G > 0$). This suggests that high temperatures favor the desorption of O_2. As can be seen from the colored solid lines on the left side of Fig. 2(c), as the temperature increases, the enthalpy difference between O_{ads} and O_2 reduces the Gibbs energy value, gradually driving the total $\Delta G < 0$ for the reaction to take place spontaneously.

Plasma catalysis

In plasma-catalytic CO_2 dissociation reactions, compared to thermal catalytic processes, CO_2 molecules are first pre-activated by plasma, as shown in Fig. 3(a). For instance, in the case of the solid green line, after being pre-activated by low levels of plasma excitation, the activation energy barrier

required for the CO_2 dissociation reaction is reduced, enabling the reaction to occur at lower temperatures. Additionally, the overall change in the reaction enthalpy also decreases by $\Delta\Delta H$.
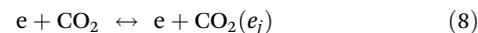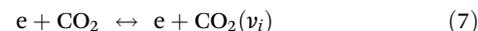
The effectiveness of plasma catalysis in reducing the reaction activation energy barrier can be attributed to its unique molecular activation pathway at the microscopic level. As shown in Fig. 3(b), compared to direct electron excitation that causes the dissociation of ground-state CO_2 molecules, high-energy electrons in the plasma initiate a V–V collision process, in which CO_2 molecules gradually transition from low-energy vibrational states to higher-energy states and eventually dissociate. This mechanism is vividly referred to as the "ladder-climbing process", where lower energy input guides the CO_2 molecules to step up their vibrational energy levels until they are activated and participate in dissociation.

Under the influence of these mechanisms, the basic reactions in plasma-activated CO_2 dissociation include:
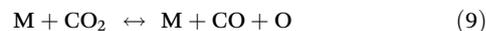
Electron impact ionization:

$$e + CO_2 \rightarrow e + e + CO_2^+ \qquad (6)$$

Electron impact excitation:

$$e + CO_2 \leftrightarrow e + CO_2(v_i) \qquad (7)$$

$$e + CO_2 \leftrightarrow e + CO_2(e_j) \qquad (8)$$

Dissociation upon collision with heavy particles:

$$M + CO_2 \leftrightarrow M + CO + O \qquad (9)$$

$$O + CO_2 \leftrightarrow O_2 + CO \qquad (10)$$

The reactions R6 to R10 constitute a primary process, where "e" represents an electron, with the energy level of e on the left side of the reaction being higher than that on the right. The notation "v_i" refers to the vibrational excitation energy levels of CO_2, typically considering both symmetric ($i = a$, b, c, d) and asymmetric levels ($1 \leq i \leq 21$). "e_j" indicates the electronic excitation energy levels of CO_2, usually considering two levels ($j = 1, 2$). "M" represents any heavy particle, such as CO_2, CO, O_2, *etc*. In addition to these reactions, several important secondary processes also occur:

Recombination of CO and O/O_2:

$$M + O + CO \leftrightarrow M + CO_2 \qquad (11)$$

$$O_2 + CO \leftrightarrow O + CO_2 \qquad (12)$$
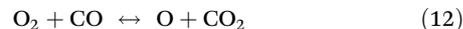
Vibrational–translational (V–T) relaxation:

$$M + CO_2(v_i) \rightarrow M + CO_2(v_x) \qquad (13)$$

Electron detachment:

$$O^- + CO \leftrightarrow CO_2 + e \qquad (14)$$
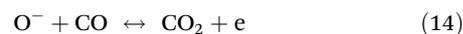
Electron attachment:

$$e + CO \leftrightarrow O^- + C \qquad (15)$$

In reactions R11 to R15, "v_x" represents a vibrational energy level that is lower than v_i.

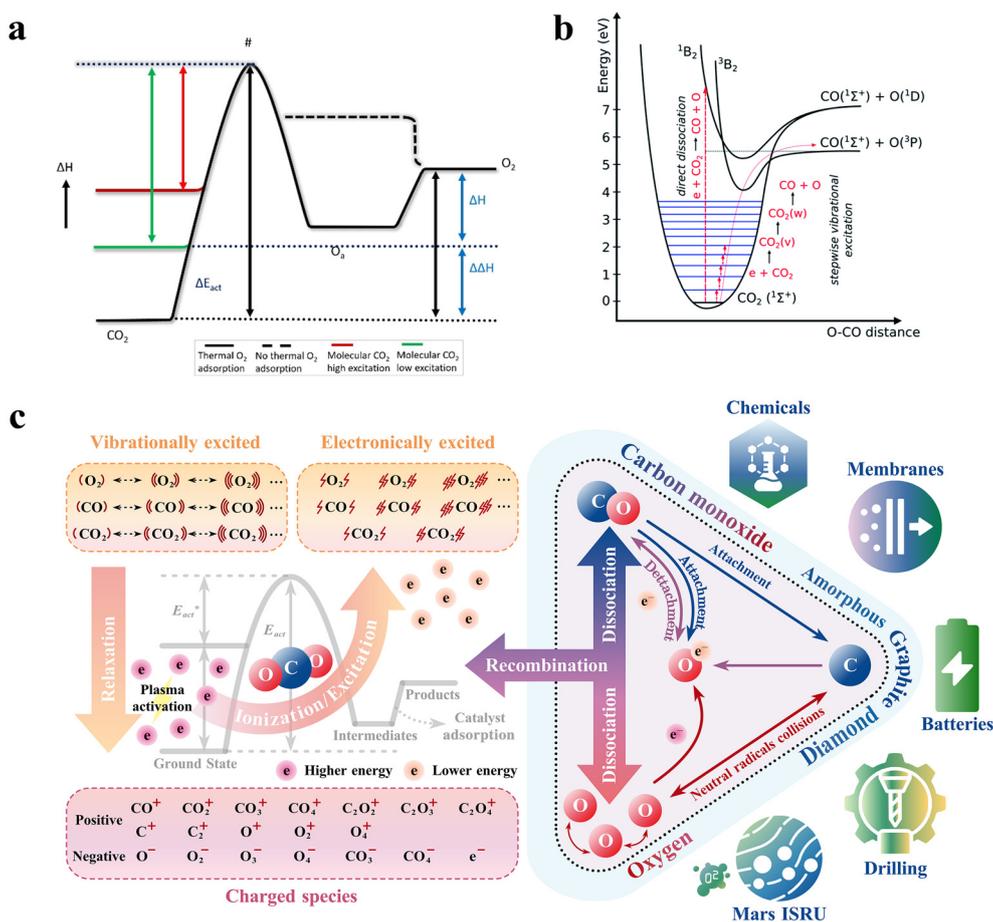**Fig. 3** Plasma catalysis of CO_2 dissociation. (a) Qualitative enthalpy plot of plasma-activation of CO_2. Reproduced from ref. 77 with permission from John Wiley and Sons, copyright 2024. (b) Schematic of part of CO_2 electronic and vibrational levels. Reproduced from ref. 80 with permission from the Royal Society of Chemistry, copyright 2015. (c) Schematic of the basic process of plasma-activated CO_2 dissociation.

Fig. 3(c) provides a detailed illustration of the interactions between the primary and secondary processes, as well as the key species and products involved in the reactions. Under the influence of high-energy electrons generated in the plasma, CO_2 molecules in their ground state undergo electron impact ionization (R6), producing CO_2^+ ions. Simultaneously, electron collisions with CO_2 molecules also lead to the formation of vibrationally excited $CO_2(v_i)$ and electronically excited $CO_2(e_j)$ species (R7 and R8). Electrons transitioning from higher to lower energy states can induce energy level upshift through V–V collisions between $CO_2(v_i)$. In addition to the formation of vibrationally and electronically excited CO_2 species, electronically excited CO and O_2 species are also generated. Furthermore, electron loss and gain during collisions between different species result in the formation of various charged intermediates, such as CO^+, O^-, and others. CO_2 molecules undergo dissociation reactions upon collisions with heavy particles, producing CO and O/O_2 species. Apart from the primary processes, secondary processes include V–T relaxation between $CO_2(v_i)$ and ground state molecules, leading to a decrease in vibrational energy levels. This

process occurs at a rate lower than that of V–V collisions, with the lost energy primarily dissipated as heat into the system. The generated CO and O/O_2 species can also undergo recombination processes, while electron adsorption and desorption between species like CO, O, O_2, C, and O^- are also significant secondary processes. Among the three products of CO_2 dissociation, CO can be further utilized to synthesize a variety of chemicals, while carbon products with various morphologies find applications in membrane technologies, battery storage, drilling, and extraction industries. O_2 holds significant value in specific scenarios, such as *in situ* resource utilization (ISRU) on Mars.

It is evident that CO_2 dissociation follows different reaction pathways in thermal catalysis and plasma catalysis systems. Taking advantage of the ability to activate CO_2 molecules efficiently at a lower energy input, LTP in combination with catalysts can significantly reduce the reaction difficulty of CO_2 dissociation. This synergy enables CO_2 conversion under milder conditions, thereby contributing to carbon reduction and the production of valuable chemicals.

Plasma setups toward promising CO$_2$ conversion performance

After reviewing current research on LTP-enabled CO$_2$ dissociation, it can be concluded that the effectiveness of CO$_2$ conversion is influenced by various plasma setups, including discharge types, power supplies, *in situ* plasma control techniques, and post-plasma coupling strategies.[71,72,81–144] As shown in the center pie chart of Fig. 4, regarding discharge forms, among the 66 relevant studies, 22 papers employed DBD plasma for CO$_2$ dissociation,[81–102] accounting for 33.33%. Research on GAD plasma[122–137] and MWD plasma[103–118] each accounted for 24.24%, with 16 papers in each category. Additionally, 4 studies explored spark discharge plasma,[71,141–143] contributing to 6.06%. Other plasma types, including corona discharge,[119,120] glow discharge,[72,138–140] non-self-sustained discharge,[121] and micro-slit discharge[144] plasma, collectively accounted for 12.12%.

Regarding the plasma power supplies, the outer ring chart of Fig. 4, marked with solid black lines, illustrates the types and proportions of plasma power supplies used to generate each discharge form. In the case of DBD plasma, alternating current (AC) power supplies are predominantly used, followed by pulsed power supplies. For GAD plasma, direct current (DC) power supplies are mainly employed, followed by AC power supplies, with some studies utilizing AC-pulsed power supplies for plasma excitation. For MWD plasma, the power supplies are primarily fixed-frequency solid-state microwave supplies, predominantly operating at 2.45 GHz, although 24 GHz and 915 MHz frequencies are also used.

In terms of *in situ* plasma regulation techniques, the second layer of the annular chart from the inside out in Fig. 4 lists the main *in situ* techniques corresponding to the three most used plasma forms. For DBD plasma, modulation towards plasma setups mainly relies on the addition of catalysts and the adjustment of dielectric properties of the barrier materials, with some studies exploring time-cycling strategies for *in situ* regulation. As for GAD plasma, magnetic fields can be applied to the discharge channel, or the vortex flow field can be created to alter the fluid dynamics distribution, thereby enabling *in situ* regulation of reaction parameters. *In situ* control strategies for MWD plasma typically focus on manipulating gas pressure and optimizing waveguide design.

As shown in the outermost ring chart of Fig. 4, post-plasma coupling strategies primarily concern reaction systems involving GAD and MWD plasma, where catalysts cannot be directly placed in the discharge region. For GAD plasma, there have been studies involving the use of catalysts or carbon beds for coupling downstream, while for MWD plasma, CO$_2$ dissociation can be enhanced through integration with electrocatalysis or quenching structures.

Plasma power supplies

Power supplies are the core components of the plasma systems, providing the necessary energy for discharge and being closely related to various discharge parameters. For the different plasma forms applied in CO$_2$ dissociation, Table 1 lists the commonly used power supplies along with their basic output parameters.

DC power sources are predominantly used to drive GAD plasma. To prevent the discharge channel from transitioning into a high-current arc mode and to avoid overheating of the reactor, a current-limiting resistor is typically added.[122] During operation, the current amplitude generally ranges from mA to A. Additionally, the GAD process involves a repetitive arc initiation–gliding–extinction cycle, and its frequently changing load characteristics place high demands on the stability of the power supply. When DC power supplies are used to drive low-intensity discharge forms such as corona discharge, glow discharge, and micro-slit discharge plasmas, the output voltage is typically low.

AC power supplies are mainly used in DBD plasma systems because the load of a DBD reactor can be approximated as a capacitor, which has a blocking effect on DC. The setting of the AC output frequency directly influences the level of power injection. Increasing the frequency while maintaining constant output voltage can increase the power, often resulting in enhanced CO$_2$ conversion. When the output power is fixed, increasing the frequency can make the discharge more uniform, but it does not necessarily promote the CO$_2$ conversion rate.[84,89]

Pulsed power supplies can facilitate a variety of plasma forms. Among them, nanosecond pulsed power supplies, with their short pulse width, low duty cycle, and high instantaneous power density brought by fast pulse rise times, offer unique advantages in terms of energy efficiency. For instance, Yong *et al.*[142] used a nanosecond pulsed power supply in spark discharge plasma for CO$_2$ dissociation, achieving a 16% CO$_2$ conversion rate with 23% energy efficiency. AC-pulsed power
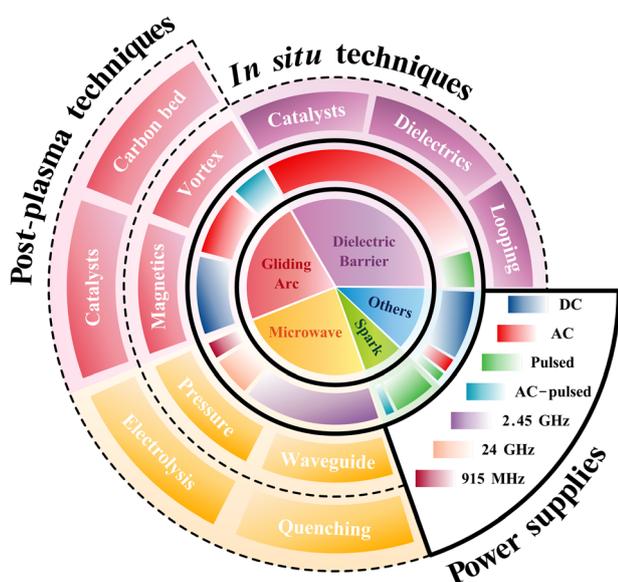

Fig. 4 Pie chart combined with a ring chart of different plasma setups.

Table 1 Commonly used plasma power supplies in CO_2 dissociation and their features

Plasma power supply	Waveform	Discharge type	Output parameters	Ref.
DC	———	GAD	▶ 5–15 kV	122, 124, 126, 129, 130, 132, 134 and 137
		Corona	▶ 8–40 W	120
		Glow	▶ 30 V	138 and 139
		Micro-slit	▶ 400–850 V	144
AC	(sine wave)	DBD	▶ 3–15 kV ▶ 4–100 kHz	81–102
		GAD	▶ 0.25–15 kV ▶ 20–60 kHz	123, 125, 127, 128, 131, 134 and 135
		Glow	▶ 2–15 kV ▶ 2–10 kHz	72 and 140
Pulsed	(square wave)	Spark	▶ 6–20 kV ▶ 30–100 kHz	141–143
		DBD	▶ 5–30 W	83
		Corona	▶ 35–51 kV ▶ 20–200 Hz	119
		Non-self-sustained	▶ 10 kV ▶ 20 kHz	121
AC-pulsed	(AC-pulsed wave)	GAD	▶ 10 kV ▶ 0.05–40 kHz	133 and 136
		Spark	▶ 10 kV ▶ 20 kHz	71
MW power supply	(MW wave)	MWD	▶ 2.45 GHz ▶ 0.2–2 kW	103, 105, 107, 109, 110 and 113–118
			▶ 24 GHz ▶ 0.4–5 kW	104, 106 and 111
			▶ 915 MHz ▶ 1–10 kW	108 and 112

supplies, which combine both AC and pulsed forms, can drive GAD and spark discharge plasmas and show promising energy efficiency.

Microwave power supplies typically have a fixed output frequency, but different waveguide and resonator configurations lead to various reflection processes. Since microwave energy directly interacts with the plasma region in the form of electromagnetic fields, power levels are typically used to assess the strength of the discharge. The output power of microwave power supplies generally ranges in the level of kilowatts (kW). Common 2.45 GHz microwave power supplies can achieve an output efficiency of around 90% (the ratio of plasma absorbed power to the total output power).[104] Increasing the frequency (e.g., to 24 GHz) can enhance the specific energy input (SEI) and plasma density, while the output efficiency may decrease.[145]

LTP can be modeled as an electrical circuit load based on the discharge form, and the degree of matching between the power supplies and the plasma load determines its output efficiency, which is essentially the conversion efficiency of electrical energy. Lisi et al.[82] considered an equivalent circuit model (ECM) that couples the internal circuit of the power supply with the load characteristics of the plasma before and after discharge. They highlighted the importance of frequency regulation in stabilizing the non-linear processes of plasma discharge.

However, current explorations on LTP-enabled CO_2 dissociation using various power supplies demonstrate insufficient analysis of the matching relationships between plasma power supplies and plasma loads (typically the plasma reactors) based on ECMs. From the perspective of efficient energy conversion, two critical challenges persist. On the one hand, the transmission efficiency of electricity from power supplies to plasma reactors, as an important determinant of effective energy utilization in electrically driven plasma processes, is frequently overlooked. This efficiency metric is particularly critical for evaluating the whole energy consumption during industrial-scale process optimization. On the other hand, plasma discharge parameters are intrinsically governed by the output characteristics of power supplies. Establishing fundamental circuit-level correlations between power supplies and plasma loads could advance the optimization of critical parameters, including power supply configurations and reactor designs. Overall, the ECMs of different plasma loads have not yet been studied systematically and in depth. For DBD plasma with planar or coaxial reactor geometries, relatively well-developed resistor-capacitor models exist, with key circuit parameters that can be determined from the Lissajous characteristics of stable discharge.[146,147] However, for plasma systems with transient and nonlinear nature (spark discharge and GAD) or complex and variable reactor geometries (MWD), it is very difficult to extract equivalent circuit parameters for ECM analysis. In these cases, computationally expensive numerical methods or electromagnetic simulations remain preferred over circuit approaches.[148–150] Nowadays, as emerging artificial intelligence (AI) technologies have catalyzed the paradigm-shifting research perspectives, which may facilitate the elucidation of source-load matching mechanisms through iterative learning of multi-dimensional parameter datasets. AI models, especially machine-learning (ML) algorithms based on various neural network frameworks, can significantly streamline the process of extracting and optimizing equivalent circuit parameters that are critical for ensuring efficient power transfer and desired frequency responses.[151,152] For future improvements toward efficient and in-depth ECM investigations, leveraging a hybrid approach that combines first-principles physics with ML algorithms to overcome analytical intractability in parameter extraction is a promising way. Such advancements could ultimately enable circuit-level optimization strategies for plasma-enabled CO_2 dissociation systems.

Moreover, the miniaturization and cost control of the power supplies used in laboratory-scale systems often represent one of the major challenges in scaling up LTP-based CO_2 dissociation systems for practical applications. Xu et al.[71]

attempted to use an improved cost-effective commercial neon power supply to drive spark discharge plasma for CO_2 dissociation, achieving a good balance between conversion rate and energy efficiency. For other plasma power supplies, deriving key electrical parameters through ECM analysis may help in the development of compact plasma power supply systems.

In situ techniques for CO_2 dissociation

DBD plasma has been extensively studied for its *in situ* regulation methods based on packed-bed reactors. It is important to note that the filling catalysts in DBD reactors often serve as components of the dielectric barrier, and thus, there is typically no clear distinction between the catalysts and the dielectric materials.

As shown in the statistical results listed in Table 2, alkaline metal oxides and various forms of SiO_2 materials (such as glass beads, quartz wool, and quartz sand) are the most commonly used packing materials in DBD reactors, with the dielectric constant being a key factor influencing the discharge characteristics after packing. A higher dielectric constant not only enhances the electric field strength within the discharge channel,[80] but also leads to an increase in T_g *via* Joule heating.[153] Xu *et al.*[86] directly filled $BaTiO_3$ beads between the electrodes, which have a relative dielectric constant of around 10 000. This allowed discharge in an originally non-breakdown gap, and after doping with Ar as the carrier gas, the conversion rate reached 36%. The addition of Ar effectively lowers the breakdown voltage, and its metastable states alter the electron energy distribution function (EEDF). The increased electron density is favorable for electron-excitation dissociation of CO_2 in DBD plasma. However, Ar dilution also consumes part of the discharge energy, so the overall energy efficiency is reduced. Further attachment of catalyst materials to the surface of materials with a high dielectric constant is proven to further enhance the CO_2 dissociation conversion effect in DBD plasma. Hosseini Rad *et al.*[91] packed glass beads coated with CeO_2 catalysts into the reactor, achieving a CO_2 conversion rate of 12.3% under 2-bar pressure, compared to 9% for the blank control, with the corresponding energy efficiency increasing from 16% to 20%.

In addition to spherical dielectric materials, the use of mesh-type porous materials in the gas gap has also shown good performance. Zhu *et al.*[92] filled a DBD reactor with porous Cu foam, which serves as an effective channel for electron and energy transfer. The resulting micro-discharges were evenly distributed within the gas gap, achieving a CO_2 conversion rate of up to 49.2%. Beyond enhancing the discharge, the packing materials can also act as sorbents for CO_2 storage, enabling time-sequenced manipulation of the plasma CO_2 dissociation process. Li *et al.*[85] used Mg/Al hydrotalcite powder with particle sizes ranging from 250 to 355 μm as a CO_2 sorbent, which was packed into two identical DBD reactors. After one reactor (A) completely absorbed CO_2, discharge was initiated within, and the products along with unreacted CO_2 were transferred to another reactor (B) for CO_2 desorption. CO_2 was then introduced into reactor B to saturate the sorbent, and after discharge and CO_2 conversion, the mixed gas was passed into reactor A to absorb unreacted CO_2. Followed by CO_2 being fed into reactor A until saturation was reached, the cycle was repeated with the steps above. With Ar dilution, a single cycle achieved a conversion rate of up to 67.44%. However, the time–space distribution process for conversion is inefficient in terms of plasma energy utilization, resulting in an energy efficiency below 1%, which is insufficient for practical applications.

The *in situ* modulation strategies aimed at enhancing the CO_2 conversion in GAD plasma primarily focus on increasing the coverage volume of the arc channel within the reactor, thereby increasing the contact probability with reactant molecules. One approach involves utilizing the electromagnetic field characteristics of the arc itself, where an external magnetic field is applied to guide the evolution of the discharge channel. Ivanov *et al.*[128] investigated the effects of different directions of applied magnetic fields on the performance of a GAD configuration with blade electrodes. The results indicated that in the magnetic-accelerated GAD configuration, the direction of the Lorentz force acting on the arc aligns with the direction of the gas flow (*i.e.*, the direction of arc propagation). This configuration shortened the time between arc ignition and extinction, resulting in higher CO_2 conversion rates at high flow rates (8–14 L min^{-1}), though with a decrease in dis-

Table 2 Packing materials used for DBD plasma-catalytic CO_2 dissociation. The conversion before and after the addition of packing materials are listed for comparison

Dielectric	Catalyst	Conversion before (%)	Conversion after (%)	Ref.
$BaTiO_3$	—	5	18	81
	Ni/SiO_2	18	24	
	—	—	36	86
	—	5.2	20	87
	—	1.3	1.7	102
Glass balls	—	—	12	83
	—	9	8	91
	CeO_2	9	12.3	
	—	12.5	16	101
SiO_2	—	—	4	93
	—	5.2	5.5	87
ZrO_2	—	5.2	5.8	
	—	5.2	19	
Al_2O_3	—	26	42	96
	—	—	4.9	93
	—	0.6	1.4	102
γ—Al_2O_3	—	14.5	16.3	97
	—	12.5	16	101
α-Al_2O_3	—	12.5	15	
Foamed Ni	—	—	48.6	92
Foamed Cu	—	—	49.2	
$Ca_{0.7}Sr_{0.3}TiO_3 + Li_2Si_2O_5$	—	—	15.5	93
$CaTiO_3$	—	12.5	20.5	101
CaO-B_2O_3-SiO_2	—	—	48.7	98
CaO	—	14.5	32.8	97
Quartz wool	—	14.5	24.5	
Quartz sand	—	14.5	15.2	
MgO	—	14.5	23.7	
Silica gel	—	12.5	14	101

Critical Review

Green Chemistry

charge stability and energy efficiency. In contrast, in the magnetically stabilized GAD configuration, the direction of the electromagnetic force was opposite to that of the gas flow, stabilizing the discharge channel within a certain range. At low flow rates (1–7 L min^{-1}), this setup achieved higher CO_2 conversion rates and energy efficiency, both of which decreased significantly as the flow rate increased. Zhang et al.[129] studied the discharge characteristics and CO_2 dissociation conversion of a magnetically assisted RGAD plasma driven by a DC power supply. Under the influence of the applied magnetic field and tangential gas inlet, the discharge channel rotated at a frequency of approximately 200 Hz, achieving CO_2 conversion rates of 4–4.4% and energy efficiencies of 16–17% at flow rates of 6–7 L min^{-1}.

Another *in situ* modulation technique for GAD plasma is the utilization of the flow field distribution induced by a turbulent vortex to interfere with the movement of the discharge channel. Compared to the effects of an external magnetic field, the influence of the vortex extends beyond the discharge channel to affect the entire reactor space and various stages of the reaction process. Nunnally et al.[134] employed a reactor structure that generated reverse vortex flow, achieving CO_2 conversion rates of 2–9% at high flow rates (14–40 L min^{-1}), with a peak energy efficiency of 43%. The key to achieving high energy efficiency was that the reverse vortex field improved the mixing of the discharge region with the reactant gas, increasing the residence time. Additionally, under the influence of the rotating gas flow, products were rapidly moved away from the core high-temperature region, thereby suppressing the extent of recombination reactions.[154] Thus, designing adjustable external magnetic fields and coupling them with appropriate vortex-generating structures may significantly enhance both the CO_2 dissociation conversion rates and energy efficiency in GAD plasma systems.

In MWD plasma systems, the *in situ* regulation methods are limited due to the fixed resonance cavity structure parameters at specific microwave frequencies. One of the key factors affecting MWD plasmas is the gas pressure, which typically needs to be low (around 0.15 atm) to maintain the plasma in a diffuse discharge form, ensuring that the system remains in a non-equilibrium state.[155] In specific scenarios with naturally low atmospheric pressures, such as in Martian ISRU, the atmospheric pressure on Mars is around 0.1 atm, and the atmosphere is composed of 96% CO_2,[156,157] making it particularly suitable for MWD processes. Kelly et al.[110] conducted MWD for CO_2 dissociation experiments in a laboratory-simulated Martian atmospheric environment, achieving CO and O_2 production rates of 76.1 g h^{-1} and 47 g h^{-1}, respectively, which are about 30 times higher than the yields of NASA's current MOXIE experiment.

Although the resonator dimensions are relatively fixed, some studies have employed surface wave excitation structures, such as coaxial waveguide and surfaguide,[158,159] to facilitate MWD. Qin et al.[105] utilized a coaxial resonator under atmospheric pressure to concentrate microwave energy within a central quartz tube to generate MWD plasma, achieving a CO_2 conver-

sion rate of 50% and an energy efficiency of 5.25%. Silva et al.[113] used a surfaguide as the microwave energy transmission medium, achieving a high local CO_2 conversion rate of 80%, though the CO_2 conversion was unevenly distributed within the quartz tube.

To sum up, the *in situ* regulation techniques for different plasma types influence discharge parameters, heat and mass transfer processes, and energy distribution to varying degrees. DBD plasma systems demonstrate inherent suitability for *in situ* modulation strategies in CO_2 dissociation systems, owing to their unique reactor configurations and discharge characteristics. The introduction of tailored dielectric packing materials enables versatile control over plasma-chemical reaction pathways, often yielding promising improvements in CO_2 conversion performance. However, current methodologies for determining the types, compositions, packing densities, and spatial distributions of the packing materials primarily rely on empirical trial-and-error approaches across extensive material libraries, lacking systematic optimization aligned with specific plasma parameters. To address this limitation, integrating AI-assisted screening protocols with targeted design strategies emerges as a promising pathway to enhance optimization efficiency.[160–163] The AI techniques for catalyst material selection have primarily relied on ML frameworks that integrate both supervised learning models, like convolutional neural networks trained on large-scale material property databases, and active learning algorithms that predict material properties. The efficacy of such AI-driven frameworks, however, is contingent upon the extraction of critical process descriptors and the establishment of sufficiently representative datasets including composition and structure–performance databases, and density functional theory-calculated data, helping identify promising materials efficiently. Similarly, AI models offer unique advantages in capturing the nonlinear dynamics of multi-component plasma systems during reactions and thus assist in determining plasma parameters that favor conversion performance.[164,165] For GAD and MWD plasmas, the reactions occurring within the discharge channels are often insufficient to significantly alter the overall conversion performance. This is due to the decline in T_g outside the plasma core region and the energy decay of active species, which leads to changes in the dominant reaction pathways in those areas. Therefore, considering modulation strategies for the post-plasma region is of significant importance for enhancing CO_2 dissociation.

Post-plasma techniques for CO_2 dissociation

For GAD plasma systems that have a higher throughput capacity, the short residence time of CO_2 in the discharge channel makes it difficult to achieve complete conversion. Therefore, post-plasma coupling with catalysts or carbon beds has been employed to further improve CO_2 dissociation. Zhang et al.[137] placed a tray containing a photocatalytic TiO_2 downstream of a blade-electrode GAD structure, as shown in Fig. 5(a). By adjusting the position of the catalyst tray, not only was reverse gas flow created to enhance CO_2 contact with the discharge region, but a plasma-catalysis synergistic effect was
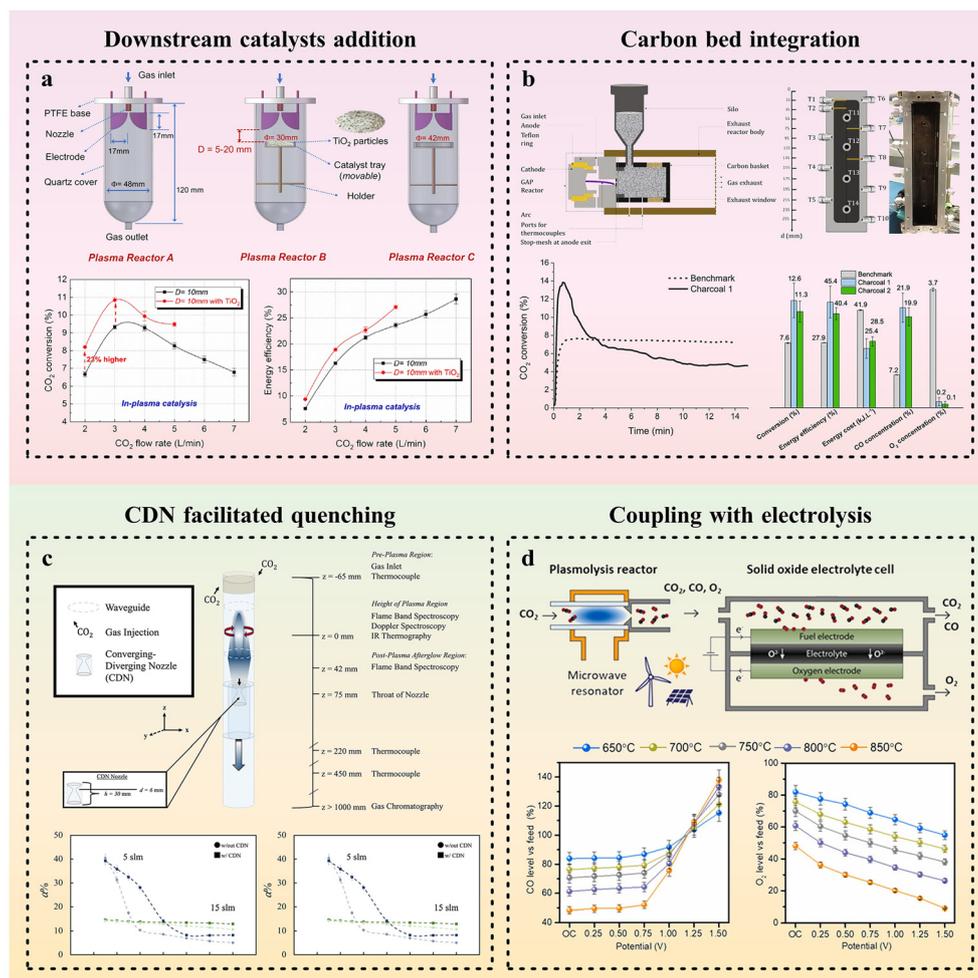
Fig. 5 Post-plasma techniques for CO_2 dissociation in GAD and MWD plasma systems. (a) Downstream catalyst addition. Reproduced from ref. 137 with permission from Springer Nature, copyright 2020. (b) Carbon bed integration in GAD plasma systems. Reproduced from ref. 125 with permission from Elsevier, copyright 2022. (c) Converging-diverging nozzle facilitated quenching. Reproduced from ref. 109 with permission from Elsevier, copyright 2023. (d) The coupling with electrolysis in MWD plasma systems. Reproduced from ref. 70 with permission from Elsevier, copyright 2022.

also achieved. Under a flow rate of 2 L min^{-1}, CO_2 conversion was increased from 4.6% to 10.8%, and energy efficiency improved from 5.4% to 12.6%. The mechanisms behind this synergy were analyzed, revealing that high-energy electrons (>3 eV) produced by the plasma could excite electron–hole pairs on the TiO_2 surface, thereby activating the catalyst and promoting CO_2 dissociation through oxygen vacancies.[166,167]

In addition to using the post-plasma energy to activate catalysts and enhance CO_2 dissociation, another important post-plasma strategy is to remove products promptly in order to promote the forward reaction based on Le Chatelier's principle.[168] As shown in Fig. 5(b), Girard-Sahun et al.[125] coupled a carbon bed with a continuous feed silo in the post-plasma region of GAD plasma, and monitored the carbon bed temperature distribution using thermocouples. The results showed that the heat generated by GAD caused O/O_2 to react with carbon (the so-called reverse Boudouard reaction) which allows the consumption of the undesirable O/O_2 and to enrich the exhaust in CO. It not only increased CO_2 conversion from

7.6% to 12.6%, but also led to a rise in CO concentration from 7.2% to 21.9%, as the removal of O/O_2 further generated CO. Overall, the energy efficiency increased from 27.9% to 45.4%. Furthermore, some studies have explored the effects of oxygen carriers to achieve complete O_2 removal in plasma chemical cycles, but a much lower throughput (0.025 L min^{-1}) was required compared to coupling with carbon beds.[169]

In MWD plasma systems, one of the challenges is addressing the decline in energy efficiency due to the excessively high T_g value in the discharge region. Specifically, in atmospheric pressure MWD processes, the T_g in the core region of the plasma torch can reach 6000 K. In the nearby regions, temperatures range from 2000 to 3000 K, which promotes the recombination of CO and O/O_2.[106] While reducing the operating pressure can help lower the T_g in the core region and reduce the temperature gradient within the reactor, it is still necessary to regulate the temperature distribution to enhance CO_2 dissociation performance. Mercer et al.[109] utilized a CDN placed at a specific position downstream of the MWD region

to generate a vortex flow geometry (Fig. 5(c)). This approach optimized the temperature field in the plasma region while enhancing the radial driving force for transporting products to the cooler downstream region, thus achieving a simultaneous improvement in both CO_2 conversion and energy efficiency. MWD plasma can also be integrated with other CO_2 conversion methods. For example, Pandiyan et al.[70] integrated an electro-catalytic process into the downstream of the MWD plasma, where a solid oxide electrolysis cell was used to further convert the CO_2, CO, and O_2 mixed gases generated by the plasma, thereby separating CO and O_2 (Fig. 5(d)). However, there is still some CO loss at present, and optimization of electrode materials is needed to improve the effective yield of CO_2 dissociation in MWD plasma coupled with electrocatalysis.

Evaluation of CO_2 conversion performance

The three typical plasma paradigms for CO_2 dissociation (DBD, GAD, and MWD plasma) have been thoroughly evaluated for their CO_2 conversion performance. To begin with, it is necessary to clarify the calculation methods for several key performance parameters:

CO_2 conversion rate:

$$X_{CO_2}\ (\%) = \frac{CO_2\ \text{converted}\ (\text{L min}^{-1})}{CO_2\ \text{inlet}\ (\text{L min}^{-1})} \times 100 \qquad (16)$$

CO production rate:

$$Y_{CO}(\text{mol h}^{-1}) = \frac{CO_2\ \text{inlet}\ (\text{L min}^{-1}) \times X_{CO_2} \times 60\ (\text{min h}^{-1})}{24.5(\text{L mol}^{-1}) \times 100} \qquad (17)$$

SEI:

$$SEI\ (\text{kJ L}^{-1}) = \frac{\text{discharge power}\ (\text{kW})}{\text{flow rate}\ (\text{L min}^{-1})} \times 60\ (\text{s min}^{-1}) \qquad (18)$$

$$\begin{aligned} SEI\ (\text{eV per molecule}) = SEI\ (\text{kJ L}^{-1}) \\ \times \frac{6.24 \times 10^{21}\ (\text{eV kJ}^{-1}) \times 24.5\ (\text{L mol}^{-1})}{6.022 \times 10^{23}\ (\text{molecule per mol})} \end{aligned} \qquad (19)$$

It should be noted that the molar value "24.5 (L mol^{-1})" in R17 and R19 is only valid at 298 K and atmospheric pressure; for other conditions, certain calibrations are required.

Energy efficiency of CO_2 dissociation (R1):

$$\begin{aligned} \eta\ (\%) &= \frac{X_{CO_2} \times \Delta H_{298}\ (\text{kJ mol}^{-1})}{SEI\ (\text{kJ L}^{-1})} \\ &= \frac{X_{CO_2} \times \Delta H_{298}\ (\text{eV per molecule})}{SEI\ (\text{eV per molecule})} \end{aligned} \qquad (20)$$

Here "ΔH_{298}" (283 kJ mol^{-1} or 2.93 eV per molecule) represents the enthalpy change of the CO_2 dissociation reaction (R1) at 298 K.

Energy cost of CO_2 dissociation (R1):

$$EC_{CO_2}\ (\text{kJ mol}_{\text{converted}}^{-1}) = \frac{SEI\ (\text{kJ L}^{-1}) \times 24.5\ (\text{L mol}^{-1}) \times 100}{X_{CO_2}} \qquad (21)$$

Based on equations R16 to R21, the CO_2 conversion performance under different plasma setups can be evaluated, with the two most critical metrics being X_{CO_2} and η. It should be noted that not all the parameters are listed by the authors, but they can be calculated using the experimental data provided in these articles, ultimately yielding all the evaluation metrics. As shown in Fig. 6(a), (c) and (e), the X_{CO_2} and η achieved by the three types of plasma systems under different SEIs are statistically summarized.

For DBD plasma, X_{CO_2} increases with the SEI, which typically exceeds 40% within the range of 3–110 eV per molecule. In terms of η, higher SEIs generally result in lower η for CO_2 dissociation. However, at lower SEIs, some studies reported η reaching around 40%. The work conducted by Wang et al.[98] accomplished the optimal balance between X_{CO_2} and η. In their study, they packed the DBD reactor with microstructured $Ca_{0.8}Sr_{0.2}TiO_3$ materials, and when the addition weight percentage was 5 wt%, X_{CO_2} and η reached 48.71% and 44.62%, respectively.

For GAD plasma-activated CO_2 dissociation, a notable difference compared to the DBD plasma system is its generally lower (less than 30%) and smaller SEI (less than 4 eV per molecule). However, it exhibits a significant advantage in terms of η, which can reach an average of 30% and a maximum of 61.55%.[123] Furthermore, Zhang et al.[122] incorporated biochar into the GAD plasma system, leveraging the synergistic effects of both plasma chemistry and thermochemistry to achieve a balance between X_{CO_2} (27.1%) and η (39.59%).

MWD plasma for CO_2 dissociation achieves the highest average X_{CO_2}, reaching approximately 34%. As the SEI increases from 0.5 to 100 eV per molecule, a significant enhancement in conversion performance is observed, with a maximum X_{CO_2} of up to 92% (with Ar dilution).[115] Furthermore, the MWD plasma also demonstrates relatively high η within the lower SEI range. Chen et al.[112] utilized surface wave excitation to drive MWD, achieving an η of up to 56% with an SEI of around 2.9 eV per molecule after coupling with a downstream NiO/TiO_2 catalyst chamber. The corresponding X_{CO_2} reached 45%, resulting in a favorable balance of CO_2 dissociation performance within this system.

Based on the estimation by Snoeckx and Bogaerts,[170] LTP-based energy conversion technologies for syngas production need to achieve an η of at least 60% in order to be competitive with existing mature processes, such as thermal catalysis and electrolysis. This η target can also be applied to the CO_2 dissociation field. While factors like renewable energy integration and modularization facilitate the competitiveness of LTP technology even below this target, it still provides a relevant benchmark. As indicated by the red dashed lines in Fig. 6(a), (c) and (e), there is still a gap between the η achieved by DBD plasma for CO_2 dissociation and this target, while GAD and MWD plasmas have already met or are close to meeting this goal. However, for MWD plasma, although there are reported results exceeding the 60% efficiency target and even reaching 90%,[155,171,172] these results were not reproducible in subsequent studies. In the recent work of van Rooij et al.,[117] they
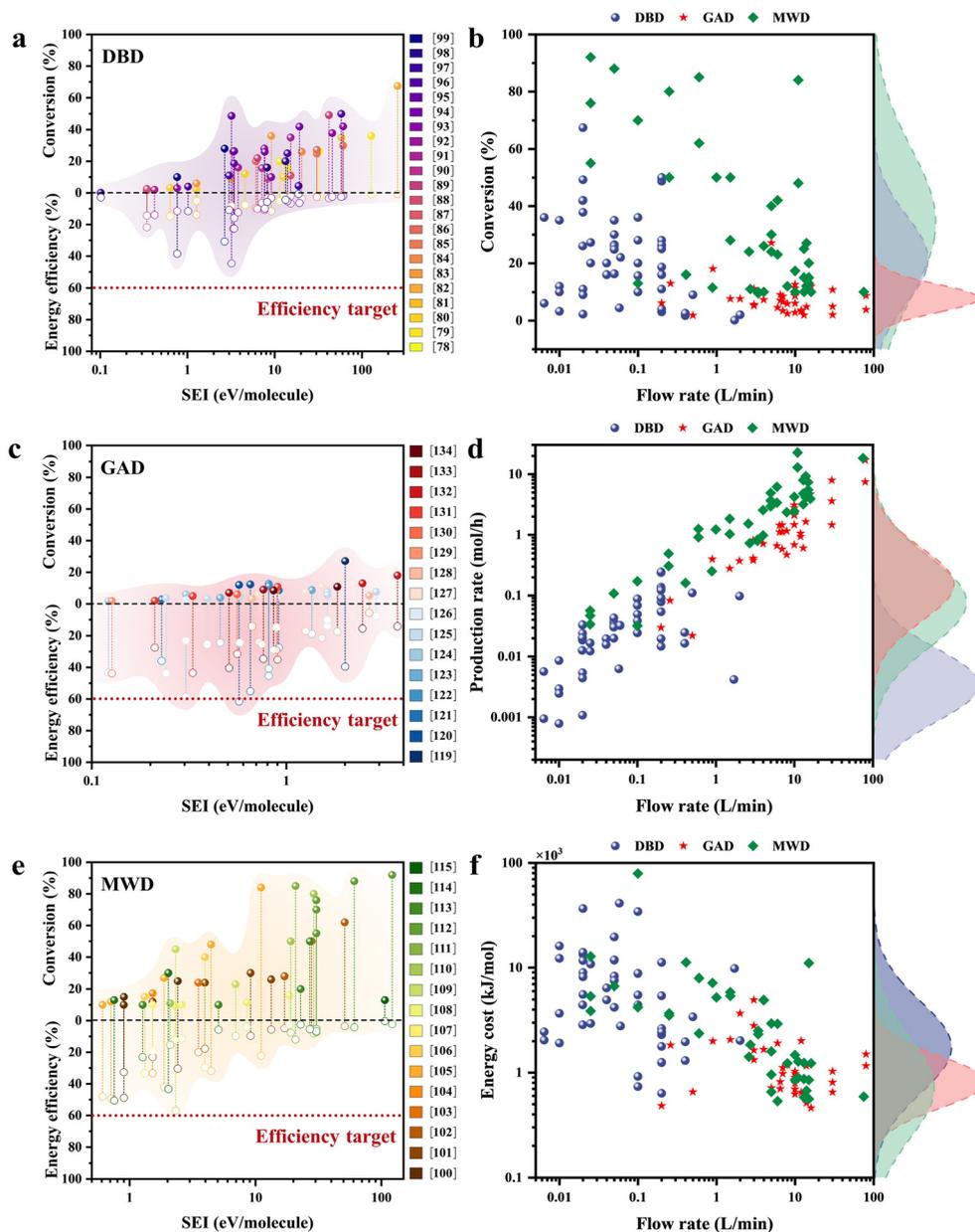
Fig. 6 Statistical analysis of the CO_2 dissociation performance of different plasma systems. The conversion and energy efficiency *versus* SEI of (a) DBD, (c) GAD, and (e) MWD plasma systems, in which the data from different articles are identified by colors shown in the side bars; the distribution of (b) conversion, (d) production rate, and (f) energy cost of DBD, GAD, and MWD plasma systems at different flow rates.

did not obtain comparable energy efficiencies (the maximum value was near 50%) using conditions like those in high-efficiency studies. It is worth noting that, with the plasma setup tailored to achieve non-equilibrium conditions throughout the whole discharge region, theoretical models indicate that the energy efficiency could reach 90% *via* the vibrational excitation mechanism.[173,174] However, because the aforementioned studies did not provide sufficient evidence to substantiate the underlying mechanism, they were not included in the statistical analysis presented in this work.

In addition to discussing the X_{CO_2} and η associated with SEI, practical energy conversion applications often focus on

the process throughput, which refers to the amount of CO_2 processed per unit of time. This is closely related to the CO_2 inlet flow rate. Therefore, we further analyzed the distribution patterns of X_{CO_2}, Y_{CO}, and EC_{CO_2} of CO_2 conversion for the three plasma forms, as shown in Fig. 6(b) and (d).

Regarding the CO_2 flow rate, the DBD plasma typically operates with an inlet flow rate of less than 1 L min^{-1}, while the flow rates in MWD and GAD plasmas can reach up to 75–80 L min^{-1}, which are significantly higher than that of the DBD plasma. With regard to X_{CO_2}, the normalized normal distribution curves of the X_{CO_2} for different plasma types are plotted on the right axis of Fig. 6(b). The peak height of these curves

corresponds to the distribution density, while the position of the peak along the vertical axis indicates the mean X_{CO_2} (expectation value). It can be observed that the X_{CO_2} distribution for MWD plasma is quite scattered, with the highest mean X_{CO_2}, while the conversion rate for DBD plasma is more concentrated, with a lower mean X_{CO_2} than that of the MWD plasma. The X_{CO_2} for GAD plasma is the most concentrated but at a lower level. However, due to the larger throughput of GAD plasma setups, the normalized log–normal distribution curve of Y_{CO} shown on the right axis of Fig. 6(d) indicates that the average Y_{CO} in GAD plasma is higher than that in the other two plasma forms, with a more concentrated distribution. The average Y_{CO} in MWD plasma is lower than that in GAD plasma but still significantly higher than that in DBD plasma.

The EC_{CO_2} metric which integrates energy consumption with X_{CO_2}, offers a new perspective for evaluating the CO_2 conversion performance of the three plasma setups. As shown in Fig. 6(f), the normalized log–normal distribution curve of EC_{CO_2} plotted on the right axis reveals that the GAD and MWD plasmas exhibit relatively similar average EC_{CO_2}. However, the EC_{CO_2} distribution for GAD plasma is more concentrated across different flow rates. In contrast, DBD plasma shows a significantly higher EC_{CO_2} compared to the other two plasma types.

In summary, GAD and MWD plasmas have demonstrated the potential for mass-scale applications in terms of energy efficiency and processing throughput in existing studies, yet there exist inherent limitations in the conversion rates of CO_2 dissociation. To achieve complete feedstock utilization, the systematic implementation of post-reaction gas recycling protocols becomes imperative. In contrast, DBD plasma demonstrates a more balanced performance concerning conversion rates and energy efficiencies. However, scaling DBD reactors may require distributed cascades to increase the processing capacity, which introduces non-trivial trade-offs: (1) increased consumption of dielectric packing materials, raising operational costs and waste management challenges; (2) potential degradation of conversion rates and energy efficiencies due to inhomogeneous field distribution and transport limitations at elevated flow rates. These scaling-induced compromises underscore the critical need for multi-objective optimization frameworks that reconcile throughput enhancement with sustained CO_2 conversion performance.

Understanding of conversion mechanisms in plasma-enabled CO_2 dissociation

Optical emission spectra

The optical emission spectroscopy, as a non-contact characterization technique, is one of the key *in situ* diagnostic methods for plasma diagnostics.

Through optical emission spectra (OES), it is not only feasible to effectively identify intermediate species involved in the

Table 3 Main species identified in OES obtained from DBD, spark discharge, and MWD plasma systems

Plasma type	Main species	Wavelength (nm)	Ref.
DBD	CO_2^+	▶ 288.6 ▶ 351 ▶ 367 ▶ 385 ▶ 434.2	82, 90,
	CO	▶ 451 ▶ 471.7 ▶ 483 ▶ 520 ▶ 561 ▶ 579 ▶ 610	99 and 100
	O	▶ 751 ▶ 777 ▶ 845	
Spark discharge	CO_2^+	▶ 288.6 ▶ 404.7 ▶ 410.9 ▶ 434.2	71
	CO	▶ 191.4–271.1 ▶ 447.9 ▶ 471.7 ▶ 483.5 ▶ 519.8 ▶ 561 ▶ 607.9	
	O	▶ 777.5 ▶ 844.7	
MWD	C_2	▶ 420–570	105, 108,
	CO	▶ 400–700	112–116
	C	▶ 249	and 118
	O	▶ 777.4 ▶ 844.6	

CO_2 dissociation process but also to calculate critical parameters such as electron density (n_e), T_v, and T_r (which reflect local T_g) by fitting specific spectral lines corresponding to species like CO, C_2, and those introduced by added carrier gases such as Ar and N_2. These parameters are closely related to the microscopic mechanisms of the CO_2 dissociation reaction.

In GAD plasma systems, due to the continuous movement of the discharge channel, OES diagnostics are generally not applicable.[175] To illustrate the differences in the CO_2 dissociation OES across different plasma systems, a comparison is made between the OES results of spark discharge plasma, which is similar to the GAD plasma form in terms of discharge parameters, and those of DBD and MWD plasmas.

As shown in Table 3, in the DBD plasma system, a significant presence of the CO_2^+ Fox–Duffendack–Barker (FDB) band system is observed, along with the Ångström band system of CO and atomic peaks of O. In the spark discharge plasma, the CO_2^+ species are nearly identical to those in DBD, but CO ($A^1\Pi \rightarrow X^1\Pi$) and CO ($c^3\Pi \rightarrow a^3\Pi$) species are also present. In the MWD plasma, the predominant species shift to the C_2 Swan band system, specifically (0, 0), (1, 0), and (0, 1), with band heads appearing at wavelengths of 516 nm, 473 nm, and 562 nm, respectively. Additionally, the CO Ångström band system is still observed in the range of 400–700 nm, along with the atomic peak of C. The differences in the composition of these species can be attributed to the varying intensities of the discharges. For instance, the formation of C_2 species in MWD plasma indicates a more intense CO_2 dissociation process under the influence of the discharge.

Time-resolved kinetics simulation

Using the plasma parameters obtained through OES diagnostics, the reaction mechanism of LTP-enabled CO_2 dissociation can be further calculated and analyzed using a zero-dimensional (0D) reaction kinetics model. The 0D model refers to an approach where the spatial distribution of particles in the reaction system is not considered, and only the time-resolved evolution of the interactions between species is taken into

account. In the analysis of the 0D reaction kinetics model, average data such as T_g, n_e, E/n, and pressure are inputted. By means of a selected set of reactions (which includes particle types, reaction sets, and the corresponding cross-sectional data), the concentration changes of various species and the distribution of possible reaction pathways are calculated. Through cross-validation with experimental results, the microscopic reaction mechanism can be inferred. This simplified process is of significant practical significance in elucidating the core conversion pathways of plasma CO_2 dissociation, particularly when dealing with complex intermediate reactions.

An in-depth review of studies on 0D reaction kinetics of CO_2 dissociation in DBD plasma,[84,86,91,173,176–179] GAD plasma,[125,132,136,175,180,181] and MWD plasma[103,107,110,117,182–184] has been conducted, summarizing the CO_2 reaction pathways in these three plasma systems as shown in Fig. 7.

As shown in the upper part of Fig. 7, in the DBD plasma system, electronic impact dissociation of CO_2 molecules is the dominant dissociation pathway. The primary mechanism involves electron collision with ground-state CO_2 molecules, leading to direct dissociation into CO and O. Additionally, CO_2 may undergo ionization, producing CO_2^+ ions, or dissociate into O^- ions. Furthermore, a small portion of CO_2^+ ions undergo dissociation through electron collisions, generating CO and O. The O/O^- species can collide with other molecules,

further generating O_2 or O_3, and O_2 may also undergo collisions with electrons, leading to the formation of O_2^- ions. The primary recombination reaction pathway involves collisions between CO and O with other molecules. This reaction mechanism results in relatively low electron energy utilization efficiency. However, filling the discharge region with dielectric materials primarily aims to increase the number of high-energy electrons during discharge, thereby promoting the dissociation of more CO_2 molecules. Although direct modeling of packed materials is not feasible within 0D models, attention to the related changes in simulation input parameters (particularly the reaction set, cross-section data, and reaction coefficients) is vital for accurately reflecting the conversion performance of DBD plasma-enabled CO_2 dissociation. In the work by Ponduri et al.,[185] the 0D simulation results were found to be in reasonable agreement with experimental observations after incorporating Itikawa's dissociation cross-section data[186] alongside the electron excitation cross sections reported by Phelps with a threshold of 7 eV.[187]

The lower left side of Fig. 7 summarizes the CO_2 dissociation mechanism in the GAD plasma, as revealed by the 0D reaction model. Unlike the DBD plasma system, the dissociation of CO_2 in the GAD reactors depends on the electronic excitation of ground-state CO_2 molecules, which undergo a V–V process to reach a vibrationally excited state (mainly in the
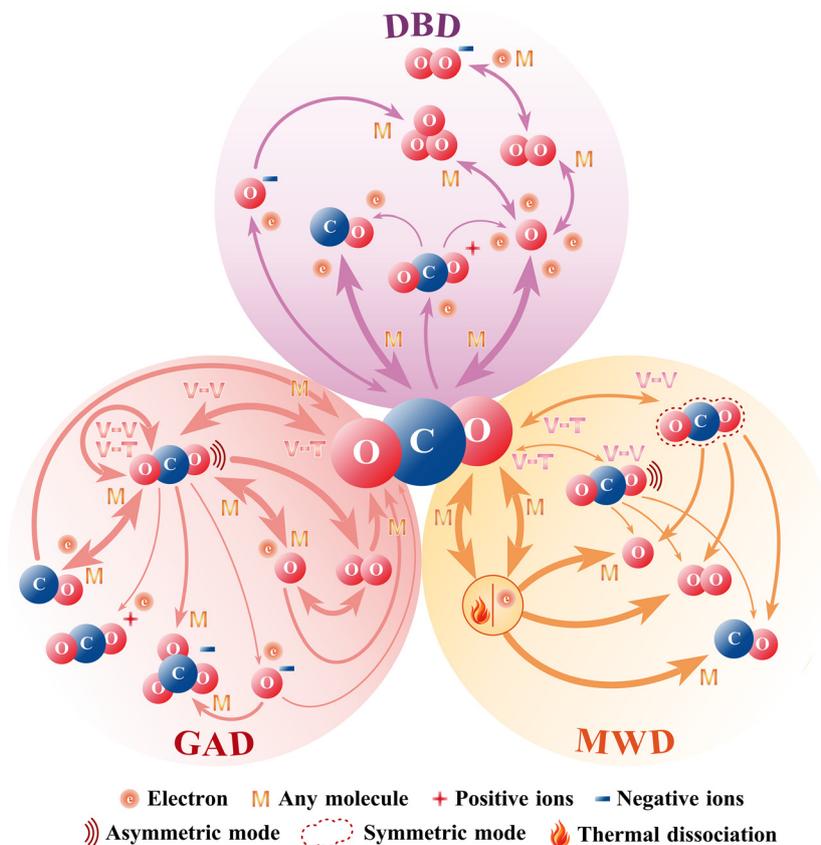

Fig. 7 Schematic overview of CO_2 dissociation mechanisms of different plasma systems. The width of the arrow line indicates the importance of the corresponding reaction path.

asymmetric mode). These vibrationally excited molecules then undergo electron collisions, resulting in the formation of CO and O particles. O can further collide with CO_2 at high-energy vibrational states to generate CO and O_2. A small number of vibrationally excited CO_2 molecules also participate in the generation of ions such as CO_2^+, CO_3^-, and O^-. The formation of CO_2 is mainly attributed to the V–T relaxation process of vibrationally excited molecules, followed by recombination through collisions between CO and O/O_2 with other particles. Through the vibrational excitation mechanism, the CO_2 dissociation path in the GAD plasma exhibits higher energy transfer efficiency. In practice, the 0D modeling results of Sun et al.[136] emphasized the importance of the vibrational-excitation mechanism in GAD plasma. The simulation outcomes exhibited good agreement with experimental measurements, indicating that the identified key species and reaction pathways offer critical guidance for deriving metrics that govern CO_2 dissociation performance. Specifically, constraining the gas temperature within the arc channel and increasing the power density serve to elevate the significance of non-equilibrium vibrational excitation in the CO_2 dissociation pathways, while facilitating the prompt removal of O atoms from the system helps suppress the recombination of CO and O. Besides, the corresponding macroscopic control strategy is primarily focused on enhancing the interaction between the plasma region and the gas flow to maximize the utilization of this efficient dissociation mechanism.

The lower right side of Fig. 7 illustrates the CO_2 dissociation path in the MWD plasma. The 0D simulation results for this system show variability under different experimental conditions. Some studies suggest that at lower pressures, CO_2 molecules dissociate primarily through vibrational excitation, mainly producing CO_2 at different vibrational modes in the symmetric form, with a small portion excited to higher energy levels in the asymmetric mode.[107,110,183] Other research indicates that at low pressures, electron-collision dissociation dominates, and as pressure increases, the discharge transitions into a torch mode. The V–T relaxation process hinders the formation of vibrationally excited species, and the dissociation mechanism shifts to one predominantly governed by thermal effects, especially involving collisions between CO_2 and O or other molecules.[178,182,184] In the work of Kozák and Annimie,[183] the 0D simulation results accurately captured the trends in CO_2 conversion and energy efficiency as functions of SEI and n_e, and the calculated T_g aligned well with experimental results. Further analysis revealed that increasing n_e and reducing T_g are critical for limiting the V–T relaxation processes that deplete vibrational levels, thereby enhancing energy efficiency. However, once the gas temperature exceeds a certain threshold, further improvements in energy efficiency become marginal, as the non-equilibrium vibrational excitation mechanism is increasingly suppressed. Therefore, when adjusting microwave discharge parameters, it is essential to carefully control operating pressure and gas flow distribution to avoid excessive heating in the plasma region, which could lead to a decrease in the energy efficiency of CO_2 dissociation.

Overall, a systematic analysis of the dominant reaction mechanisms governing CO_2 dissociation across distinct plasma systems reveals critical modality-specific energy transfer pathways. In DBD plasma systems, CO_2 dissociation predominantly proceeds via direct electron-impact dissociation mediated by high-energy electrons, whereas GAD and MWD plasma systems additionally exploit vibrational excitation mechanisms targeting ground-state CO_2 molecules. This distinction in energy transfer strategies underpins the superior energy efficiency observed in GAD and MWD systems compared to DBD systems.

Combining the plasma setups and the corresponding conversion performances, it further elucidates the following mechanistic drivers: DBD reactors can achieve elevated CO_2 conversion rates through high-energy electrons generated from synergistic interactions between plasma and the packing materials, where material defects provide abundant active sites to lower dissociation activation barriers. However, the energy efficiency of DBD systems remains constrained by the inherent limitations of electron-impact dissociation requiring excessive energy inputs (SEI > 100 eV per molecule) that poorly exploit injected power.

In GAD plasma systems, the gliding discharge channels allow sufficient contact with CO_2 molecules, enabling effective dissociation at higher flow rates. Meanwhile, the increase of energy input becomes challenging (SEI < 10 eV per molecule) with elevated processing throughputs. Nonetheless, the energy efficiencies remain high due to the effective utilization of vibrational excitation mechanisms.

MWD plasma systems can effectively leverage electromagnetic energy from microwave power supplies to achieve high energy inputs (SEI > 100 eV per molecule), thus enabling promising CO_2 conversion rates. But their energy efficiencies undergo a drastic decline under elevated pressure conditions (>100 Torr). This degradation stems from a mechanistic transition in CO_2 dissociation pathways from vibrationally excited to electron-impact dissociation and thermally driven processes. Consequently, this pressure-dependent efficiency collapse confines their applicability to low-pressure operational regimes, limiting the practical applications.

Space-resolved dynamics modeling

In the CO_2 dissociation process within the plasma reactor, the discharge channel and other regions of the reactor typically exhibit different reaction conditions. The precise control of the conversion process cannot be fulfilled without considering the effects of spatial distribution. Therefore, multi-physics field modeling and simulation are employed to study the factors influencing the CO_2 conversion process. This approach helps in understanding the spatial variations in temperature, pressure, and plasma characteristics, which are critical for optimizing reactor performance and enhancing CO_2 dissociation.

The dimension of the simulation model often determines its proximity to the real multi-physics field. Commonly used simulation models in the literature can be classified into one-

dimensional (1D), two-dimensional (2D), and three-dimensional (3D) models. As shown in Fig. 8, the 1D model simplifies the spatial distribution of multi-physics fields to a single degree of freedom, typically applied to uniform discharge modes or idealized simplified physical processes. For instance, Ponduri et al.[185] equated the plasma region between symmetric parallel plate electrodes of DBD to a 1D model and studied the effect of flow and temperature distribution on CO_2 dissociation conversion. In the case of GAD plasma, Wang et al.[188] simplified the discharge channels within parallel plates and expanding electrodes, constructing two types of 1D models along the gas propagation direction to simulate the multi-physics field of GAD. MWD plasma can also be approximated by a 1D multi-physics model. Berthelot et al.[189] simplified the energy injection in the MWD region of a cylindrical reactor to a power pulse and combined it with the temperature field along the axial direction to form a simplified 1D model.

The 2D multi-physics model is typically used in axisymmetric or rotationally symmetric discharge structures, as it can better fit the field distribution of actual discharge processes. For example, in a DBD reactor with dielectric material packing, a 1D model fails to embody the micro-discharges between dielectric particles. However, by modeling the basic unit consisting of electrodes, dielectric layers, filling particles, and gas gaps in 2D, the spatial distribution of the electric field can be well approximated.[96] For the blade-electrode structure in GAD, a 2D model established for the plane where the GAD occurs, with appropriate initial and boundary conditions, can effectively represent both the discharge initiation area and the propagation region of the arc channel.[190] In a spark discharge plasma reactor with rotating-symmetric needle-plate electrodes, modeling the vertical half cross-section in 2D allows for the physical field distribution of the entire space to be derived.[71]

When the model dimension is further increased to 3D, the accuracy of the multi-physics field evolution process in the spatial domain is further enhanced. Taking a packed bed DBD reactor as an example, Van Laer et al.[174] established a 3D multi-physics field model of a reactor unit, which validated the electric field enhancement effect of the dielectric packing. For plasma reactors with more complex multi-physics processes, such as GAD[137] and MWD,[109] the 3D models developed are nearly identical to the actual reactor structures and can resolve details that are often overlooked by 1D or 2D models. Although the 3D modeling configurations of the GAD and MWD plasma systems bear certain resemblances to their respective reactor geometries, they differ significantly in the way their multi-physics parameters are prescribed. For the blade-structured GAD reactor illustrated, the electromagnetic boundary conditions closely mirror those used in the analogous 2D model. However, when coupling the electromagnetic field with the thermal and flow fields, the presence of the electrodes and the underlying tray, with each defined by its unique geometry and material properties, modulates heat and mass transfer. It further leads to spatial variations in temperature and gas velocity that, in turn, alter the evolution of the discharge channel. In contrast, the MWD plasma system, which operates in an electrodeless discharge mode, is typically simulated by focusing on the spatial propagation and distribution of the electromagnetic field. For a reactor of fixed dimensions, this yields a discharge region that remains essentially stationary. In the case of the converging-diverging nozzle shown, the
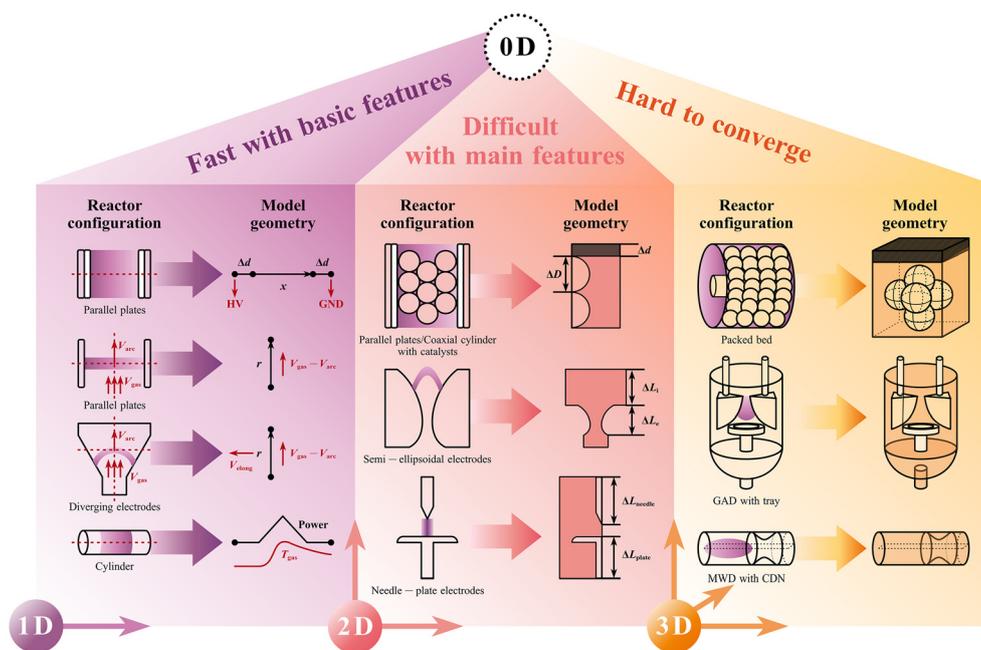

Fig. 8 Multi-physics modeling of CO_2 dissociation in different plasma systems. The basic reactor configuration and model geometry of 1D, 2D, and 3D multi-physics modeling methods are illustrated from left to right, while the coupling features of each method are listed above.

tangential gas inlet induces a disturbed vortex flow, characterized by counter-rotating eddies that effectively mitigate thermal hot spots within the discharge zone.

Practically, the macroscopic physical laws fitted by the aforementioned multi-physics field models need to be further integrated with the microscopic reaction mechanisms calculated through 0D reaction kinetics, as discussed before. While the increased complexity of multi-physics field models brings them closer to actual physical processes, it also introduces challenges in coupling with 0D models. Currently, 1D models can be effectively coupled with 0D simulation calculations. However, in 2D models, the inclusion of reaction kinetics significantly increases the computational difficulty. As for 3D models, due to the excessive number of variables and constraints, it is still difficult to achieve a coupling with 0D models while maintaining the accuracy of the multi-physics field model.

In the development of plasma-assisted CO_2 dissociation technologies for scale-up applications, multi-physics modeling serves as an indispensable analytical tool during the preliminary reactor design and operational monitoring to post-deployment maintenance phases. However, such modeling methodologies remain in their nascent stages of development.

The 0D kinetic simulations with temporal evolution of reaction mechanisms provide foundational insights into plasma-chemical pathways, which can be integrated with 1D multi-physics models for simplified reactor geometries under quasi-steady-state plasma discharges, enabling the incorporation of macroscopic transport phenomena (*e.g.*, thermal gradients and species diffusion) into conversion performance analyses. Advancing to 2D modeling significantly enhances fidelity to physical realities through spatially resolved field distributions, albeit at the cost of exponentially increased computational complexity and convergence challenges. The coupling of 3D multi-physics simulations with 0D reaction kinetics currently faces prohibitive barriers due to incompatible temporal-spatial resolution requirements and unaccounted multi-scale plasma heterogeneities. The complexity of incorporating detailed reaction mechanisms into higher-dimensional models necessitates simplifications to make them computationally feasible.

Future progress demands dual advancements: (1) fundamental breakthroughs in plasma-specific reaction mechanisms through *in situ* diagnostics of critical parameters and (2) development of adaptive mesh algorithms capable of bridging disparate timescales. Such innovations will enable the transition from low-dimensional kinetic models to high-fidelity 3D simulations that holistically optimize CO_2 dissociation systems across molecular to reactor scales.

Techno-economic feasibility toward scale-up valorization

The LTP-enabled CO_2 dissociation technology shows promising potential for scale-up applications, yet its techno-economic feasibility still needs to be evaluated in detail. Fundamentally, critical techno-economic and performance thresholds are required when assessing the scalability. The primary benchmark lies in the CO_2 conversion performance. According to the estimation of van Rooij *et al.*,[191] a minimum single-pass CO_2 conversion target of 15–30% to mitigate the cost of downstream separation (such as pressure/temperature swing adsorption, PSA/TSA, and membrane separation) is essential. Strategies like reactor staging with intermediate O_2 removal or sorption-enhanced designs can boost conversion but introduce sorbent regeneration and durability concerns. Current energy efficiencies exhibit significant variations across different LTP systems: DBD reactors typically achieve 10–45% energy efficiency for CO_2 dissociation, while GAD or MWD reactors can reach up to 60% efficiency in specific configurations. Additionally, while LTP systems benefit from energy cost elimination associated with compression and heating, the wall-plug efficiency encompassing power supply output, plasma generation, and auxiliary systems like vacuum pumps is important for techno-economic analyses (TEA). High-frequency DBD supplies can exceed 95% efficiency but are limited to a few kW per tube,[192] GAD systems using low-frequency switching supplies reach 85–90% efficiency with individual units typically operating at 10–15 kW,[193] while MWD magnetrons can offer microwave coupling efficiency close to 100% but reduced by vacuum pumps, which leads to 70–75% wall-plug efficiency.[194]

The inherent small gas throughput presents a fundamental scalability challenge for current LTP reactors. Under laboratory conditions, DBD units process only 0.4–1.0 L min^{-1} CO_2, GAD reactors handle around 15 L min^{-1}, and MWD setups reach 15–30 L min^{-1}. All of them are orders of magnitude below conventional chemical plant feed rates of hundreds of kg h^{-1}, necessitating extensive parallelization.[195] Modularization is thus the primary scale-up strategy, envisioning thousands of DBD tubes or hundreds of GAD units sharing manifolds, or parallel MWD reactors.[191] Detz and van der Zwaan[196] also concluded that no real economy of scale existed for MWD systems since the capital cost scales linearly with the total output capacity, favoring small to midsize modular plants. However, uniform power distribution, balancing between flow and temperature, and maintenance complexity remain significant hurdles.

From the perspective of economic viability, the cost per mole of CO produced is a key metric for energy and economic assessment. For DBD systems, a high SEI of about 30 MJ mol^{-1} translates to €0.4–0.7 per mol CO which counts for the operational expenditure (OPEX), with the levelized cost of electricity (LCOE) at €0.05–0.08 per kWh from wind and photovoltaic (PV) energy.[197] Moreover, the capital expenditure (CAPEX) of a DBD system at a pilot scale of 144 kW was estimated at €1300 per kW, while the CAPEX estimated for a multi-tube DBD reactor at a flow rate of 100 m^3 h^{-1} would increase linearly with tube numbers and the power consumed.[198] Conversely, GAD systems achieve higher efficiencies. A recent TEA study by Osorio-Tejada *et al.*[199] calculated a GAD system

with a downstream carbon bed that consumed 19.5 GJ per ton (0.55 MJ mol^{-1}) of the CO produced, corresponding to a production cost at $671 per ton, lower than the equivalent electrolysis of $962 per ton. Meanwhile, the CAPEX of pilot GAD systems was envisioned at about €2400 per kW, which can be applied to plants processing up to 1000 ton per year of CO_2. As for MWD plasma systems, while they demonstrate significant advantages in energy efficiency (>50% at reduced pressure), the high CAPEX poses a potential threat to scalability. The work by O'Modhrain et al.[126] concluded that a 20 000 ton per year MWD plant would need around €7000 per kW with 3 MW generators.

On the other hand, comprehensive lifecycle assessment (LCA) addressing the holistic sustainability and environmental impacts of LTP technology provides essential metrics for evaluating the scale-up viability. A cradle-to-gate LCA comparing LTP-based and electrolytic CO production (each produced 100 ton per day of CO) found that the plasma route consumed 40% less total energy.[200] While CO_2 feedstock dominated impacts (60–80%), the plasma process showed environmental advantages over fossil-based CO in 7 out of 10 categories (e.g., 86% lower acidification, 91% lower freshwater ecotoxicity, and 83% lower fossil resource use) and a 7% lower global warming potential (GWP). Electrolysis, though offering moderate reductions in some categories, incurred an 8% higher GWP than the conventional processes.

The integration with renewable energy sources like solar and wind is a key potential advantage of LTP toward practical applications. LTP systems offer inherent modularity, enabling deployment matching local renewable capacity without massive single units. Utilizing low-marginal-cost renewable electricity significantly lowers OPEX. Against the backdrop of "net-zero" targets, anticipated rises in carbon taxes and higher carbon pricing in emissions trading systems (ETS) will further boost the competitiveness of renewable energy, thereby driving the deployment of LTP technology. For example, the economic competitiveness of MWD systems over conventional thermocatalytic processes using natural gas will occur by 2050 with a carbon price of €150 per t CO_2.[196] However, continuous CO_2 feed requires buffering or storage if plasma operates only during surplus power, and downstream processing must accommodate intermittent input. While TEA suggests fuel costs could approach €2–3 per L under direct coupling with very cheap renewables, the low capacity factor risks capital underutilization. Realizing the economic potential hinges on continued research and development to improve efficiency, reduce capital and operational costs, develop robust catalysts and reactors, and lower renewable energy prices, alongside solutions for managing variable operation and product separation. Overall, while current costs are high, LTP-driven CO_2 dissociation demonstrates potential techno-economic and environmental advantages over electrolytic or thermocatalytic routes, particularly when integrated with low-cost renewable electricity and targeted for specific modular applications.

Conclusions and perspectives

This review provides an in-depth analysis of the current research status in the field of LTP-enabled CO_2 dissociation. We first explored and compared the differences between thermal catalysis and plasma catalysis processes in CO_2 dissociation, focusing particularly on macro-level plasma setups and micro-level CO_2 dissociation mechanisms, aiming to provide a deeper understanding of the underlying principles and guiding future research directions toward scale-up applications.

At the macro level, we observed that the characteristics of different plasma power supplies lead to distinct plasma parameters. The control strategies for CO_2 dissociation processes can mainly be divided into in situ and post-plasma approaches. For DBD plasma, in situ techniques focus on the use of various medium materials within the reactor. For GAD plasma, plasma regulation is achieved by introducing external magnetic fields or a vortex to alter the heat and mass transfer in the reaction zone. MWD plasma, on the other hand, can adjust the gas pressure and waveguide structure to modulate the distribution of microwave energy. In terms of post-plasma techniques, improving the conversion of high-throughput GAD plasma often requires the use of post-plasma catalysts or carbon beds. MWD plasma can optimize the temperature field by adding a nozzle and can also be coupled with electrocatalytic processes to enhance conversion. After comparing the CO_2 conversion performance of different plasma forms, we observed that GAD and MWD plasmas have advantages in balancing processing throughput and energy consumption.

At the microscopic level, plasma parameters were obtained through in situ diagnostics using OES. Current research attempts to clarify the reaction mechanisms of CO_2 dissociation in different types of plasmas from both 0D reaction kinetics and multi-physics simulation perspectives. For the representative plasma forms, namely DBD, GAD, and MWD plasma, the core CO_2 dissociation pathways are centered around electronic excitation collision dissociation, vibrational excitation dissociation, and electronic or thermal effect-dominated dissociation, respectively. As for multi-physics simulations within LTP reactors, although 3D models offer the highest degree of accuracy in reflecting actual conditions, coupling with 0D models still requires simplification of the physical field spatial distribution using 1D or 2D models, through which the computational complexity can be reduced while maintaining reasonable accuracy.

From a detailed techno-economic perspective encompassing CO_2 conversion performance, CO production costs, and benefits of renewable-energy integration, GAD and MWD plasma systems already demonstrate promising CO_2 conversion rates and energy efficiencies. However, further reductions in capital and operational costs are essential during the modularization processes. Upon coupling with renewables, the economic competitiveness of LTP technology is projected to become increasingly prominent alongside global decarbonization efforts, with the potential to outper-
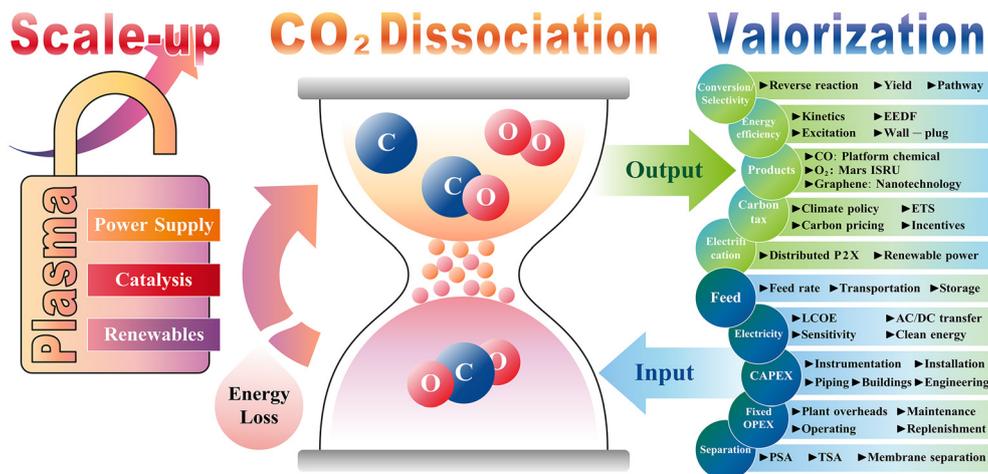
Fig. 9 Techno-economic view of unlocking scale-up CO_2 dissociation with plasma technology.

form mature CO_2 valorization routes such as electrolysis and thermal catalysis.

Based on the key findings above, we believe that the LTP-based CO_2 dissociation technology has the potential for broader adoption and mass-scale applications. As shown in Fig. 9, on the one hand, LTP technology needs specialized design in several areas, such as power supply improvements (compact modularization, adaptation to various load characteristics), catalytic coupling (development of plasma-specific catalysts, *in situ*/post-coupling strategies), and renewable energy systems (integrated system solutions). On the other hand, in the full-process LTP technology for valorization of CO_2 dissociation, there are multiple layers of techno-economic constraints.[201,202] The key breakthrough for scaling up the applications of plasma technology lies in the balance of various process indicators and improvement of its competitiveness. Upon considering the entire process flow of plasma-assisted CO_2 dissociation technology, from the perspective of the upstream input, it necessitates the comprehensive evaluation of feed supply and separation, electricity, and construction/maintenance costs. At the midstream plasma conversion section, it is imperative to synergistically investigate discharge configurations and reactor geometries to elucidate reaction mechanisms while employing diverse characterization techniques to monitor real-time reaction states. This integrated approach aims to minimize energy loss during the conversion process. For downstream product management, it is vital to achieve optimal processing throughput while enhancing overall energy efficiency. Furthermore, the strategic development of application scenarios compatible with LTP technology should be prioritized. Concurrently, preparatory work for scale-up applications requires alignment with future policies that support CO_2 valorization technologies and adaptation to renewable energy-driven electrification transition trends. This multi-scale optimization framework bridges fundamental plasma physics with practical engineering implementation requirements.

Conflicts of interest

There are no conflicts to declare.

Data availability

All the data are available within the article.

Acknowledgements

References

1 T. R. Karl and K. E. Trenberth, *Science*, 2003, **302**, 1719–1723.

2 C. Hepburn, E. Adlen, J. Beddington, E. A. Carter, S. Fuss, N. Mac Dowell, J. C. Minx, P. Smith and C. K. Williams, *Nature*, 2019, **575**, 87–97.

3 Y.-M. Wei, K. Chen, J.-N. Kang, W. Chen, X.-Y. Wang and X. Zhang, *Engineering*, 2022, **14**, 52–63.

4 X. Zhao, X. Ma, B. Chen, Y. Shang and M. Song, *Resour., Conserv. Recycl.*, 2022, **176**, 105959.

5 R. C. Rial, *Renewable Sustainable Energy Rev.*, 2024, **196**, 114369.

6 J. J. Sheng, *Modern Chemical Enhanced Oil Recovery: Theory and Practice*, Gulf Professional Publishing, 2010.

7 R. Safi, R. K. Agarwal and S. Banerjee, *Chem. Eng. Sci.*, 2016, **144**, 30–38.

8 R. Farajzadeh, A. A. Eftekhari, G. Dafnomilis, L. W. Lake and J. Bruining, *Appl. Energy*, 2020, **261**, 114467.

9 J. Jiang, Z. Rui, R. Hazlett and J. Lu, *Appl. Energy*, 2019, **247**, 190–211.

10 A. Mustafa, B. G. Lougou, Y. Shuai, Z. Wang and H. Tan, *J. Energy Chem.*, 2020, **49**, 96–123.

11 S.-Y. Pan, P.-C. Chiang, W. Pan and H. Kim, *Crit. Rev. Environ. Sci. Technol.*, 2018, **48**, 471–534.

12 D. J. Davidson, *Nat. Energy*, 2019, **4**, 254–256.

13 U. Bhattarai, T. Maraseni and A. Apan, *Sci. Total Environ.*, 2022, **833**, 155159.

14 P. A. Østergaard, N. Duic, Y. Noorollahi and S. A. Kalogirou, *Renewable Energy*, 2021, **179**, 877–884.

15 S. J. Davis, N. S. Lewis, M. Shaner, S. Aggarwal, D. Arent, I. L. Azevedo, S. M. Benson, T. Bradley, J. Brouwer, Y.-M. Chiang, C. T. M. Clack, A. Cohen, S. Doig, J. Edmonds, P. Fennell, C. B. Field, B. Hannegan, B.-M. Hodge, M. I. Hoffert, E. Ingersoll, P. Jaramillo, K. S. Lackner, K. J. Mach, M. Mastrandrea, J. Ogden, P. F. Peterson, D. L. Sanchez, D. Sperling, J. Stagner, J. E. Trancik, C.-J. Yang and K. Caldeira, *Science*, 2018, **360**, eaas9793.

16 J. Rogelj, O. Geden, A. Cowie and A. Reisinger, *Nature*, 2021, **591**, 365–368.

17 J. Huo, Z. Wang, C. Oberschelp, G. Guillén-Gosálbez and S. Hellweg, *Green Chem.*, 2023, **25**, 415–430.

18 C. Gao and Y. Xiong, *Chin. J. Chem.*, 2022, **40**, 153–159.

19 Z. Zhang, P. Yi, S. Hu and Y. Jin, *J. Environ. Manage.*, 2023, **340**, 118010.

20 I. Sorrenti, T. B. Harild Rasmussen, S. You and Q. Wu, *Renewable Sustainable Energy Rev.*, 2022, **165**, 112380.

21 F. V. Vázquez, J. Koponen, V. Ruuskanen, C. Bajamundi, A. Kosonen, P. Simell, J. Ahola, C. Frilund, J. Elfving, M. Reinikainen, N. Heikkinen, J. Kauppinen and P. Piermartini, *J. CO$_2$ Util.*, 2018, **28**, 235–246.

22 J. Farfan, M. Fasihi and C. Breyer, *J. Cleaner Prod.*, 2019, **217**, 821–835.

23 J. Wang, M. S. AlQahtani, X. Wang, S. D. Knecht, S. G. Bilén, C. Song and W. Chu, *Green Chem.*, 2021, **23**, 1642–1647.

24 A. Modak, P. Bhanja, S. Dutta, B. Chowdhury and A. Bhaumik, *Green Chem.*, 2020, **22**, 4002–4033.

25 L. E. Heim, H. Konnerth and M. H. G. Prechtl, *Green Chem.*, 2017, **19**, 2347–2355.

26 L. C. Grabow and M. Mavrikakis, *ACS Catal.*, 2011, **1**, 365–384.

27 G. Liu, G. Yang, X. Peng, J. Wu and N. Tsubaki, *Chem. Soc. Rev.*, 2022, **51**, 5606–5659.

28 A. M. Appel, J. E. Bercaw, A. B. Bocarsly, H. Dobbek, D. L. DuBois, M. Dupuis, J. G. Ferry, E. Fujita, R. Hille, P. J. A. Kenis, C. A. Kerfeld, R. H. Morris, C. H. F. Peden, A. R. Portis, S. W. Ragsdale, T. B. Rauchfuss, J. N. H. Reek, L. C. Seefeldt, R. K. Thauer and G. L. Waldrop, *Chem. Rev.*, 2013, **113**, 6621–6658.

29 P. Kumar and D. S. Monder, *J. Phys. Chem. C*, 2024, **128**, 15451–15463.

30 X. Nie, W. Luo, M. J. Janik and A. Asthagiri, *J. Catal.*, 2014, **312**, 108–122.

31 Z. Xiao, P. Li, H. Zhang, S. Zhang, X. Tan, F. Ye, J. Gu, J. Zou and D. Wang, *Fuel*, 2024, **362**, 130906.

32 A. Galadima and O. Muraza, *Renewable Sustainable Energy Rev.*, 2019, **115**, 109333.

33 S. De, A. Dokania, A. Ramirez and J. Gascon, *ACS Catal.*, 2020, **10**, 14147–14185.

34 C. A. H. Price, T. R. Reina and J. Liu, *J. Energy Chem.*, 2021, **57**, 304–324.

35 Z. Wang, H. Song, H. Liu and J. Ye, *Angew. Chem., Int. Ed.*, 2020, **59**, 8016–8035.

36 P.-P. Yang and M.-R. Gao, *Chem. Soc. Rev.*, 2023, **52**, 4343–4380.

37 S. Zhang, Q. Fan, R. Xia and T. J. Meyer, *Acc. Chem. Res.*, 2020, **53**, 255–264.

38 T. H. T. Myren, A. Alherz, J. R. Thurston, T. A. Stinson, C. G. Huntzinger, C. B. Musgrave and O. R. Luca, *ACS Catal.*, 2020, **10**, 1961–1968.

39 J.-J. Velasco-Vélez, T. Jones, D. Gao, E. Carbonio, R. Arrigo, C.-J. Hsu, Y.-C. Huang, C.-L. Dong, J.-M. Chen, J.-F. Lee, P. Strasser, B. Roldan Cuenya, R. Schlögl, A. Knop-Gericke and C.-H. Chuang, *ACS Sustainable Chem. Eng.*, 2019, **7**, 1485–1492.

40 A. J. Morris, R. T. McGibbon and A. B. Bocarsly, *ChemSusChem*, 2011, **4**, 191–196.

41 A. Bogaerts and G. Centi, *Front. Energy Res.*, 2020, **8**, 111.

42 H. Radhakrishnan, S. Gnangbe, A. Duereh, S. U. I. Uday, A. Lusi, H. Hu, H. Hu, M. M. Wright and X. Bai, *Green Chem.*, 2024, **26**, 9156–9175.

43 P. Lamichhane, N. Pourali, L. Scott, N. N. Tran, L. Lin, M. E. Gelonch, E. V. Rebrov and V. Hessel, *Renewable Sustainable Energy Rev.*, 2024, **189**, 114044.

44 M. S. Cha and R. Snoeckx, *Front. Mech. Eng.*, 2022, **8**, 903379.

45 L. Dou, Y. Liu, Y. Gao, J. Li, X. Hu, S. Zhang, K. (Ken) Ostrikov and T. Shao, *Appl. Catal., B*, 2022, **318**, 121830.

46 Y. Gao, L. Dou, S. Zhang, L. Zong, J. Pan, X. Hu, H. Sun, K. (Ken) Ostrikov and T. Shao, *Chem. Eng. J.*, 2021, **420**, 127693.

47 M. Y. Ong, *J. Cleaner Prod.*, 2022, **336**, 130447.

48 J. P. Trelles, *J. Phys. D: Appl. Phys.*, 2022, **55**, 103001.

49 S. Li, G. D. Felice, S. Eichkorn, T. Shao and F. Gallucci, *Plasma Sci. Technol.*, 2024, **26**, 094001.

50 T. Shao, S. Zhang, C. Zhang, Y. Gao, H. Sun, L. Dou and D. Xi, *Proc. CSEE*, 2024, **44**, 7453–7479.

51 S. Ullah, Y. Gao, L. Dou, Y. Liu, T. Shao, Y. Yang and A. B. Murphy, *Plasma Chem. Plasma Process.*, 2023, **43**, 1335–1383.

52 T. Li, Y. Gao, R. Zhou, T. Zhang and K. (Ken) Ostrikov, *Curr. Opin. Green Sustainable Chem.*, 2024, **47**, 100915.

53 S. Liu, L. R. Winter and J. G. Chen, *ACS Catal.*, 2020, **10**, 2855–2871.

54 B. Zhao, Y. Liu, Z. Zhu, H. Guo and X. Ma, *J. CO$_2$ Util.*, 2018, **24**, 34–39.

55 A. Lebouvier, S. A. Iwarere, P. d'Argenlieu, D. Ramjugernath and L. Fulcheri, *Energy Fuels*, 2013, **27**, 2712–2722.

56 L. D. Pietanza, G. Colonna and M. Capitelli, *Plasma Phys. Controlled Fusion*, 2023, **65**, 044004.

57 B. Ashford and X. Tu, *Curr. Opin. Green Sustainable Chem.*, 2017, **3**, 45–49.

58 Y. Luo, X. Yue, H. Zhang, X. Liu and Z. Wu, *Sci. Total Environ.*, 2024, **906**, 167486.

59 Y. Yin, T. Yang, Z. Li, E. Devid, D. Auerbach and A. W. Kleyn, *Phys. Chem. Chem. Phys.*, 2021, **23**, 7974–7987.

60 B. Wanten, R. Vertongen, R. De Meyer and A. Bogaerts, *J. Energy Chem.*, 2023, **86**, 180–196.

61 R. Vertongen and A. Bogaerts, *J. CO₂ Util.*, 2023, **72**, 102510.

62 G. Trenchev, A. Nikiforov, W. Wang, St. Kolev and A. Bogaerts, *Chem. Eng. J.*, 2019, **362**, 830–841.

63 Y. Uytdenhouwen, K. M. Bal, I. Michielsen, E. C. Neyts, V. Meynen, P. Cool and A. Bogaerts, *Chem. Eng. J.*, 2019, **372**, 1253–1264.

64 D. Mei, Y.-L. He, S. Liu, J. Yan and X. Tu, *Plasma Processes Polym.*, 2016, **13**, 544–556.

65 S. Xu, H. Chen, C. Hardacre and X. Fan, *J. Phys. D: Appl. Phys.*, 2021, **54**, 233001.

66 Y. Zhang, B. Wang, Z. Ji, Y. Jiao, Y. Shao, H. Chen and X. Fan, *Chem. Eng. J.*, 2023, **465**, 142855.

67 A. George, B. Shen, M. Craven, Y. Wang, D. Kang, C. Wu and X. Tu, *Renewable Sustainable Energy Rev.*, 2021, **135**, 109702.

68 X. Gong, Y. Lin, X. Li, A. Wu, H. Zhang, J. Yan and C. Du, *J. Air Waste Manage. Assoc.*, 2020, **70**, 138–157.

69 J. Ananthanarasimhan, R. Lakshminarayana, M. S. Anand and S. Dasappa, *Plasma Sources Sci. Technol.*, 2019, **28**, 085012.

70 A. Pandiyan, V. Kyriakou, D. Neagu, S. Welzel, A. Goede, M. C. M. van de Sanden and M. N. Tsampas, *J. CO₂ Util.*, 2022, **57**, 101904.

71 Y. Xu, Y. Gao, D. Xi, L. Dou, C. Zhang, B. Lu and T. Shao, *Ind. Eng. Chem. Res.*, 2023, **62**, 15872–15883.

72 S. L. Brock, M. Marquez, S. L. Suib, Y. Hayashi and H. Matsumoto, *J. Catal.*, 1998, **180**, 225–233.

73 Q. Huang, D. Zhang, D. Wang, K. Liu and A. W. Kleyn, *J. Phys. D: Appl. Phys.*, 2017, **50**, 294001.

74 C. E. Bartosch, L. J. Whitman and W. Ho, *J. Chem. Phys.*, 1986, **85**, 1052–1060.

75 Q. Ge and M. Neurock, *J. Phys. Chem. B*, 2006, **110**, 15368–15380.

76 L. Liu, C. Zhao and Y. Li, *J. Phys. Chem. C*, 2012, **116**, 7904–7912.

77 L. Lefferts, *Angew. Chem., Int. Ed.*, 2024, **63**, e202305322.

78 Y. Xu, A. V. Ruban and M. Mavrikakis, *J. Am. Chem. Soc.*, 2004, **126**, 4717–4725.

79 C. E. Wartnaby, A. Stuck, Y. Y. Yeo and D. A. King, *J. Phys. Chem.*, 1996, **100**, 12483–12488.

80 A. Bogaerts, T. Kozák, K. Van Laer and R. Snoeckx, *Faraday Discuss.*, 2015, **183**, 217–232.

81 K. Zhang, G. Zhang, X. Liu, A. N. Phan and K. Luo, *Ind. Eng. Chem. Res.*, 2017, **56**, 3204–3216.

82 N. Lisi, U. Pasqual Laverdura, R. Chierchia, I. Luisetto and S. Stendardo, *Sci. Rep.*, 2023, **13**, 7394.

83 D. Yap, J.-M. Tatibouët and C. Batiot-Dupeyrat, *J. CO₂ Util.*, 2015, **12**, 54–61.

84 R. Aerts, W. Somers and A. Bogaerts, *ChemSusChem*, 2015, **8**, 702–716.

85 S. Li and F. Gallucci, *Chem. Eng. J.*, 2022, **430**, 132979.

86 S. Xu, J. C. Whitehead and P. A. Martin, *Chem. Eng. J.*, 2017, **327**, 764–773.

87 I. Michielsen, Y. Uytdenhouwen, J. Pype, B. Michielsen, J. Mertens, F. Reniers, V. Meynen and A. Bogaerts, *Chem. Eng. J.*, 2017, **326**, 477–488.

88 S. Paulussen, B. Verheyde, X. Tu, C. D. Bie, T. Martens, D. Petrovic, A. Bogaerts and B. Sels, *Plasma Sources Sci. Technol.*, 2010, **19**, 034015.

89 D. Mei and X. Tu, *J. CO₂ Util.*, 2017, **19**, 68–78.

90 D. Khunda, S. Li, N. Cherkasov, M. Z. M. Rishard, A. L. Chaffee and E. V. Rebrov, *React. Chem. Eng.*, 2023, **8**, 2223–2233.

91 R. Hosseini Rad, V. Brüser, M. Schiorlin, J. Schäfer and R. Brandenburg, *Chem. Eng. J.*, 2023, **456**, 141072.

92 S. Zhu, A. Zhou, F. Yu, B. Dai and C. Ma, *Plasma Sci. Technol.*, 2019, **21**, 085504.

93 R. Li, Q. Tang, S. Yin and T. Sato, *Fuel Process. Technol.*, 2006, **87**, 617–622.

94 A. Ozkan, A. Bogaerts and F. Reniers, *J. Phys. D: Appl. Phys.*, 2017, **50**, 084004.

95 A. Ozkan, T. Dufour, T. Silva, N. Britun, R. Snyders, A. Bogaerts and F. Reniers, *Plasma Sources Sci. Technol.*, 2016, **25**, 025013.

96 K. Van Laer and A. Bogaerts, *Energy Technol.*, 2015, **3**, 1038–1044.

97 X. Duan, Z. Hu, Y. Li and B. Wang, *AIChE J.*, 2015, **61**, 898–903.

98 S. Wang, Y. Zhang, X. Liu and X. Wang, *Plasma Chem. Plasma Process.*, 2012, **32**, 979–989.

99 I. Belov, S. Paulussen and A. Bogaerts, *Plasma Sources Sci. Technol.*, 2016, **25**, 015023.

100 F. Brehmer, S. Welzel, M. C. M. van de Sanden and R. Engeln, *J. Appl. Phys.*, 2014, **116**, 123303.

101 Q. Yu, M. Kong, T. Liu, J. Fei and X. Zheng, *Plasma Chem. Plasma Process.*, 2012, **32**, 153–163.

102 T. Butterworth, R. Elder and R. Allen, *Chem. Eng. J.*, 2016, **293**, 55–67.

103 N. den Harder, D. C. M. van den Bekerom, R. S. Al, M. F. Graswinckel, J. M. Palomares, F. J. J. Peeters, S. Ponduri, T. Minea, W. A. Bongers, M. C. M. van de Sanden and G. J. van Rooij, *Plasma Processes Polym.*, 2016, **14**, 1600120.

104 D. Mansfeld, S. Sintsov, N. Chekmarev and A. Vodopyanov, *J. CO₂ Util.*, 2020, **40**, 101197.

105 Y. Qin, G. Niu, X. Wang, D. Luo and Y. Duan, *Chem. Phys.*, 2020, **538**, 110913.

106 N. V. Chekmarev, D. A. Mansfeld, A. V. Vodopyanov, S. V. Sintsov, E. I. Preobrazhensky and M. A. Remez, *J. CO₂ Util.*, 2024, **82**, 102759.

107 S. Kelly, E. Mercer, Y. Gorbanev, I. Fedirchyk, C. Verheyen, K. Werner, P. Pullumbi, A. Cowley and A. Bogaerts, *J. CO₂ Util.*, 2024, **80**, 102668.

108 W. Bongers, H. Bouwmeester, B. Wolf, F. Peeters, S. Welzel, D. van den Bekerom, N. den Harder, A. Goede, M. Graswinckel, P. W. Groen, J. Kopecki, M. Leins, G. van Rooij, A. Schulz, M. Walker and R. van de Sanden, *Plasma Processes Polym.*, 2017, **14**, 1600126.

109 E. R. Mercer, S. Van Alphen, C. F. A. M. van Deursen, T. W. H. Righart, W. A. Bongers, R. Snyders, A. Bogaerts, M. C. M. van de Sanden and F. J. J. Peeters, *Fuel*, 2023, **334**, 126734.

110 S. Kelly, C. Verheyen, A. Cowley and A. Bogaerts, *Chem*, 2022, **8**, 2797–2816.

111 N. V. Chekmarev, D. A. Mansfeld, S. V. Sintsov, E. I. Preobrazhenskii, A. V. Vodopyanov, A. P. Fokin and A. A. Ananichev, in *2024 Photonics & Electromagnetics Research Symposium (PIERS)*, IEEE, Chengdu, China, 2024, pp. 1–5.

112 G. Chen, T. Godfroid, N. Britun, V. Georgieva, M.-P. Delplancke-Ogletree and R. Snyders, *Appl. Catal., B*, 2017, **214**, 114–125.

113 T. Silva, N. Britun, T. Godfroid and R. Snyders, *Plasma Processes Polym.*, 2017, **14**, e1600103.

114 T. Silva, N. Britun, T. Godfroid and R. Snyders, *Plasma Sources Sci. Technol.*, 2014, **23**, 025009.

115 M. Tsuji, T. Tanoue, K. Nakano and Y. Nishimura, *Chem. Lett.*, 2001, **30**, 22–23.

116 L. F. Spencer and A. D. Gallimore, *Plasma Sources Sci. Technol.*, 2012, **22**, 015019.

117 G. J. van Rooij, D. C. M. van den Bekerom, N. den Harder, T. Minea, G. Berden, W. A. Bongers, R. Engeln, M. F. Graswinckel, E. Zoethout and M. C. M. van de Sanden, *Faraday Discuss.*, 2015, **183**, 233–248.

118 A. Vesel, M. Mozetic, A. Drenik and M. Balat-Pichelin, *Chem. Phys.*, 2011, **382**, 127–131.

119 Y. Wen and X. Jiang, *Plasma Chem. Plasma Process.*, 2001, **21**, 665–678.

120 W. Xu, M.-W. Li, G.-H. Xu and Y.-L. Tian, *Jpn. J. Appl. Phys.*, 2004, **43**, 8310–8311.

121 S. N. Andreev, V. V. Zakharov, V. N. Ochkin and S. Yu. Savinov, *Spectrochim. Acta, Part A*, 2004, **60**, 3361–3369.

122 H. Zhang, Q. Tan, Q. Huang, K. Wang, X. Tu, X. Zhao, C. Wu, J. Yan and X. Li, *ACS Sustainable Chem. Eng.*, 2022, **10**, 7712–7725.

123 S. C. Kim, M. S. Lim and Y. N. Chun, *Plasma Chem. Plasma Process.*, 2014, **34**, 125–143.

124 M. Ramakers, J. A. Medrano, G. Trenchev, F. Gallucci and A. Bogaerts, *Plasma Sources Sci. Technol.*, 2017, **26**, 125002.

125 F. Girard-Sahun, O. Biondo, G. Trenchev, G. van Rooij and A. Bogaerts, *Chem. Eng. J.*, 2022, **442**, 136268.

126 C. O'Modhrain, G. Trenchev, Y. Gorbanev and A. Bogaerts, *ACS Eng. Au*, 2024, **4**, 333–344.

127 H. Xu, Z. Wei, Y. Huang, M. Qiao, H. Zhang, M. Shao and K. Xie, *Chem. Eng. Sci.*, 2024, **299**, 120527.

128 V. Ivanov, Ts. Paunska, S. Lazarova, A. Bogaerts and St. Kolev, *J. CO₂ Util.*, 2023, **67**, 102300.

129 H. Zhang, L. Li, X. Li, W. Wang, J. Yan and X. Tu, *J. CO₂ Util.*, 2018, **27**, 472–479.

130 L. Li, H. Zhang, X. Li, X. Kong, R. Xu, K. Tay and X. Tu, *J. CO₂ Util.*, 2019, **29**, 296–303.

131 D. Nagassou, S. Mohsenian, M. Nallar, P. Yu, H.-W. Wong and J. P. Trelles, *J. CO₂ Util.*, 2020, **38**, 39–48.

132 M. Ramakers, G. Trenchev, S. Heijkers, W. Wang and A. Bogaerts, *ChemSusChem*, 2017, **10**, 2642–2652.

133 J.-L. Liu, H.-W. Park, W.-J. Chung and D.-W. Park, *Plasma Chem. Plasma Process.*, 2016, **36**, 437–449.

134 T. Nunnally, K. Gutsol, A. Rabinovich, A. Fridman, A. Gutsol and A. Kemoun, *J. Phys. D: Appl. Phys.*, 2011, **44**, 274009.

135 A. Indarto, D. R. Yang, J.-W. Choi, H. Lee and H. K. Song, *J. Hazard. Mater.*, 2007, **146**, 309–315.

136 S. R. Sun, H. X. Wang, D. H. Mei, X. Tu and A. Bogaerts, *J. CO₂ Util.*, 2017, **17**, 220–234.

137 H. Zhang, L. Li, R. Xu, J. Huang, N. Wang, X. Li and X. Tu, *Waste Disposal Sustainable Energy*, 2020, **2**, 139–150.

138 E. F. Mendez-Martinez, P. G. Reyes, D. Osorio-Gonzalez, F. Castillo and H. Martinez, *Plasma Sci. Technol.*, 2010, **12**, 314–319.

139 P. G. Reyes, E. F. Mendez, D. Osorio-Gonzalez, F. Castillo and H. Martínez, *Phys. Status Solidi C*, 2008, **5**, 907–910.

140 J.-Y. Wang, G.-G. Xia, A. Huang, S. L. Suib, Y. Hayashi and H. Matsumoto, *J. Catal.*, 1999, **185**, 152–159.

141 C. Montesano, T. P. W. Salden, L. M. Martini, G. Dilecce and P. Tosi, *J. Phys. Chem. C*, 2023, **127**, 10045–10050.

142 T. Yong, H. Zhong, E. Pannier, C. Laux and M. A. Cappelli, *Plasma Sources Sci. Technol.*, 2023, **32**, 115012.

143 M. S. Bak, S.-K. Im and M. Cappelli, *IEEE Trans. Plasma Sci.*, 2015, **43**, 1002–1007.

144 T. Ma, H.-X. Wang, Q. Shi, S.-N. Li and A. B. Murphy, *Plasma Sources Sci. Technol.*, 2018, **27**, 075011.

145 S. Sintsov, K. Tabata, D. Mansfeld, A. Vodopyanov and K. Komurasaki, *J. Phys. D: Appl. Phys.*, 2020, **53**, 305203.

146 A. V. Pipa, J. Koskulics, R. Brandenburg and T. Hoder, *Rev. Sci. Instrum.*, 2012, **83**, 115112.

147 T. Tamida, R. Nagata and T. Itani, *Electr. Eng. Jpn.*, 2023, **143**, e23455.

148 K.-J. Chung, S. Lee, Y. S. Hwang and C. Y. Kim, *Curr. Appl. Phys.*, 2015, **15**, 977–986.

149 A. Sawicki and M. Haltof, *Przegl. Elektrotech.*, 2016, **1**, 195–198.

150 R. Miotk, M. Jasiński and J. Mizeraczyk, *IOP Conf. Ser.: Mater. Sci. Eng.*, 2016, **113**, 012008.

151 D. Lee, G. Shin, S. Lee, K. Kim, T.-H. Oh and H.-J. Song, *IEEE Trans. Microwave Theory Tech.*, 2022, **70**, 4726–4739.

152 Z. Dai, J. Pang, M. Li, Q. Li, J. Peng and S. He, *IEEE Trans. Microwave Theory Tech.*, 2020, **68**, 3278–3286.

153 J. Kruszelnicki, K. W. Engeling, J. E. Foster and M. J. Kushner, *J. Phys. D: Appl. Phys.*, 2020, **54**, 104001.

154 A. Gutsol and J. A. Bakken, *J. Phys. D: Appl. Phys.*, 1998, **31**, 704–711.

155 A. Fridman, *Plasma Chemistry*, Cambridge University Press, 2008.

156 R. M. Haberle, R. T. Clancy, F. Forget, M. D. Smith and R. W. Zurek, *The Atmosphere and Climate of Mars*, Cambridge University Press, 2017.

157 H. B. Franz, M. G. Trainer, M. H. Wong, H. L. K. Manning, J. C. Stern, P. R. Mahaffy, S. K. Atreya, M. Benna, P. G. Conrad, D. N. Harpold, L. A. Leshin, C. A. Malespin, C. P. McKay, J. Thomas Nolan and E. Raaen, *Planet. Space Sci.*, 2014, **96**, 99–113.

158 M. Chaker, M. Moisan and Z. Zakrzewski, *Plasma Chem. Plasma Process.*, 1986, **6**, 79–96.

159 M. Moisan and Z. Zakrzewski, *J. Phys. D: Appl. Phys.*, 1991, **24**, 1025–1048.

160 J. Benavides-Hernández and F. Dumeignil, *ACS Catal.*, 2024, **14**, 11749–11779.

161 Y. Shen, C. Fu, W. Luo, Z. Liang, Z.-R. Wang and Q. Huang, *Green Chem.*, 2023, **25**, 7605–7611.

162 Q. Yang, Y. Fan, J. Zhou, L. Zhao, Y. Dong, J. Yu and D. Zhang, *Green Chem.*, 2023, **25**, 7216–7233.

163 L. Zhang, Q. Bing, H. Qin, L. Yu, H. Li and D. Deng, *Matter*, 2025, **8**, 102138.

164 J. Pan, Y. Liu, S. Zhang, X. Hu, Y. Liu and T. Shao, *Energy Convers. Manage.*, 2023, **277**, 116620.

165 J. Li, J. Xu, E. Rebrov and A. Bogaerts, *Chem. Eng. J.*, 2025, **507**, 159897.

166 D. Mei, X. Zhu, C. Wu, B. Ashford, P. T. Williams and X. Tu, *Appl. Catal., B*, 2016, **182**, 525–532.

167 Y.-Q. Cao, X.-R. Zhao, J. Chen, W. Zhang, M. Li, L. Zhu, X.-J. Zhang, D. Wu and A.-D. Li, *Sci. Rep.*, 2018, **8**, 12131.

168 W. P. Jorissen, *Chem. Rev.*, 1929, **6**, 17–43.

169 Y. Long, X. Wang, H. Zhang, K. Wang, W.-L. Ong, A. Bogaerts, K. Li, C. Lu, X. Li, J. Yan, X. Tu and H. Zhang, *JACS Au*, 2024, **4**, 2462–2473.

170 R. Snoeckx and A. Bogaerts, *Chem. Soc. Rev.*, 2017, **46**, 5805–5863.

171 R. I. Asisov, A. A. Fridman, V. K. Givotov, E. G. Krasheninnikov, B. I. Patrushev, B. V. Potapkin, V. D. Rusanov and M. F. Krotov, in *5th International Symposium on Plasma Chemistry (ISPC)*, Edinburgh, Scotland, 1981, pp. 774–779.

172 R. I. Azizov, A. K. Vakar, V. K. Zhivotov, M. F. Krotov, O. A. Zinov'ev, B. V. Potapkin, A. A. Rusanov, V. D. Rusanov and A. A. Fridman, *Proc. Acad. Sci. USSR, Chem. Technol. Sect.*, 1983, **271**, 94–98.

173 A. Bogaerts, A. Berthelot, S. Heijkers, S. Kolev, R. Snoeckx, S. Sun, G. Trenchev, K. V. Laer and W. Wang, *Plasma Sources Sci. Technol.*, 2017, **26**, 063001.

174 K. Van Laer and A. Bogaerts, *Plasma Sources Sci. Technol.*, 2015, **25**, 015002.

175 W. Wang, D. Mei, X. Tu and A. Bogaerts, *Chem. Eng. J.*, 2017, **330**, 11–25.

176 M. Alliati, D. Mei and X. Tu, *J. CO₂ Util.*, 2018, **27**, 308–319.

177 W. Huang, W. Yue, Y. Dong, Q. Lu, C. Shi, L. Sun, Y. Shi, Y. Chen and Y. Zhao, *Fuel*, 2023, **353**, 129236.

178 T. Kozák and A. Bogaerts, *Plasma Sources Sci. Technol.*, 2014, **23**, 045004.

179 A. Bogaerts, W. Wang, A. Berthelot and V. Guerra, *Plasma Sources Sci. Technol.*, 2016, **25**, 055016.

180 H. Zhang, H. Zhang, G. Trenchev, X. Li, Y. Wu and A. Bogaerts, *Plasma Sources Sci. Technol.*, 2020, **29**, 045019.

181 S. R. Sun, H. X. Wang and A. Bogaerts, *Plasma Sources Sci. Technol.*, 2020, **29**, 025012.

182 A. Berthelot and A. Bogaerts, *J. Phys. Chem. C*, 2017, **121**, 8236–8251.

183 T. Kozák and A. Bogaerts, *Plasma Sources Sci. Technol.*, 2014, **24**, 015024.

184 D. C. M. van den Bekerom, J. M. P. Linares, T. Verreycken, E. M. van Veldhuizen, S. Nijdam, G. Berden, W. A. Bongers, M. C. M. van de Sanden and G. J. van Rooij, *Plasma Sources Sci. Technol.*, 2019, **28**, 055015.

185 S. Ponduri, M. M. Becker, S. Welzel, M. C. M. Van De Sanden, D. Loffhagen and R. Engeln, *J. Appl. Phys.*, 2016, **119**, 093301.

186 Y. Itikawa, *J. Phys. Chem. Ref. Data*, 2002, **31**, 749–767.

187 Phelps Database, (https://www.lxcat.net), (Accessed: 1 June 2025).

188 W. Wang, A. Berthelot, S. Kolev, X. Tu and A. Bogaerts, *Plasma Sources Sci. Technol.*, 2016, **25**, 065012.

189 A. Berthelot and A. Bogaerts, *Plasma Sources Sci. Technol.*, 2016, **25**, 045022.

190 S. Kolev and A. Bogaerts, *Plasma Sources Sci. Technol.*, 2014, **24**, 015025.

191 G. J. van Rooij, H. N. Akse, W. A. Bongers and M. C. M. van de Sanden, *Plasma Phys. Controlled Fusion*, 2017, **60**, 014019.

192 J. I.-Z. Chen, *Engineering*, 2011, **3**, 331–339.

193 A. Rabinovich, G. Nirenberg, S. Kocagoz, M. Surace, C. Sales and A. Fridman, *Plasma Chem. Plasma Process.*, 2022, **42**, 35–50.

194 C. K. Kiefer, R. Antunes, A. Hecimovic, A. Meindl and U. Fantz, *Chem. Eng. J.*, 2024, **481**, 148326.

195 U. Kogelschatz, *J. Phys. D: Appl. Phys.*, 2017, **50**, 051001.

196 R. J. Detz and B. Van Der Zwaan, *J. Energy Chem.*, 2022, **71**, 507–513.

197 G. Bachner, K. W. Steininger, K. Williges and A. Tuerk, *Renewable Energy*, 2019, **134**, 1369–1380.

198 H. Lamberts-Van Assche, G. Thomassen and T. Compernolle, *J. CO₂ Util.*, 2022, **64**, 102156.

199 J. Osorio-Tejada, M. Escriba-Gelonch, R. Vertongen, A. Bogaerts and V. Hessel, *Energy Environ. Sci.*, 2024, **17**, 5833–5853.

200 M. Escribà-Gelonch, J. Osorio-Tejada, R. Vertongen, A. Bogaerts and V. Hessel, *J. Cleaner Prod.*, 2025, **488**, 144578.

201 Y. Yang and A. B. Murphy, *Curr. Opin. Green Sustainable Chem.*, 2025, **51**, 100994.

202 T. Shao, Y. Yang, X. Tu and A. B. Murphy, Fundam. Res., 2025. DOI: 10.1016/j.fmre.2025.03.017, in press.